PHYSICAL REVIEW D **86,** 014032 (2012)

Unquenching the gluon propagator with Schwinger-Dyson equations

A. C. Aguilar,[1] D. Binosi,[2] and J. Papavassiliou[3]

[1]*Universidade Estadual de Campinas-UNICAMP, Instituto de Física Gleb Wataghin, 13083-859 Campinas, SP, Brazil*

[2]*European Centre for Theoretical Studies in Nuclear Physics and Related Areas (ECT*) and Fondazione Bruno Kessler, Villa Tambosi, Strada delle Tabarelle 286, I-38123 Villazzano (TN), Italy*

[3]*Department of Theoretical Physics and IFIC, University of Valencia and CSIC, E-46100, Valencia, Spain*

(Received 17 April 2012; published 27 July 2012)

In this article we use the Schwinger–Dyson equations to compute the nonperturbative modifications caused to the infrared finite gluon propagator (in the Landau gauge) by the inclusion of a small number of quark families. Our basic operating assumption is that the main bulk of the effect stems from the ''one-loop dressed'' quark loop contributing to the full gluon self-energy. This quark loop is then calculated, using as basic ingredients the full quark propagator and quark-gluon vertex; for the quark propagator we use the solution obtained from the quark-gap equation, while for the vertex we employ suitable Ansätze, which guarantee the transversality of the answer. The resulting effect is included as a correction to the quenched gluon propagator, obtained in recent lattice simulations. Our main finding is that the unquenched propagator displays a considerable suppression in the intermediate momentum region, which becomes more pronounced as we increase the number of active quark families. The influence of the quarks on the saturation point of the propagator cannot be reliably computed within the present scheme; the general tendency appears to be to decrease it, suggesting a corresponding increase in the effective gluon mass. The renormalization properties of our results, and the uncertainties induced by the unspecified transverse part of the quark-gluon vertex, are discussed. Finally, the gluon propagator is compared with the available unquenched lattice data, showing rather good agreement.

DOI: 10.1103/PhysRevD.86.014032 PACS numbers: 12.38.Aw, 12.38.Lg, 14.70.Dj

I. INTRODUCTION

In recent years considerable progress has been made in our understanding of various aspects of the nonperturbative dynamics of Yang–Mills theories, through the fruitful combination of a variety of approaches and techniques [1–28]. Particularly successful in this effort has been the continuous interplay between lattice simulations and Schwinger–Dyson equations (SDEs) [29–34], which has led to a firmer grasp on the infrared (IR) behavior of the fundamental Green's functions of QCD, such as gluon, ghost, and quark propagators, as well as some of the basic vertices of the theory, for special kinematic configurations [35–37].

A significant part of the existing SDE analysis has focused on the study of various aspects of the aforementioned Green's functions at the level of pure gauge Yang–Mills theories, i.e., without the inclusion of quarks [15,21,25]. This tendency has been mainly motivated by the fact that the vast majority of lattice simulations work in the quenched limit, making no reference to effects stemming from dynamical quarks [1,7,9].

The transition from pure $SU(3)$ Yang–Mills Green's functions to those of real world QCD is, of course, highly nontrivial and has been the focal point of relatively few lattice investigations [5,6]. At the level of the SDEs, to the best of our knowledge, this issue has been studied in detail [38,39] only in the context of the so-called ''scaling solutions'' [12], but no analogous investigation has been carried out for the (IR finite) massive solutions [40], found both in the lattice simulations and in several of the analytic studies cited above.

The purpose of the present article is to provide a self-consistent framework for addressing this latter problem in the continuum, at the level of the corresponding SDEs. In particular, we will present an approximate method for ''unquenching'' the (IR finite) gluon propagator (in the Landau gauge), computing nonperturbatively the effects induced by a small number of light quark families.

The method we present consists of two basic steps: (i) computing the fully dressed quark-loop diagram [see graph (a_{11}) in Fig. 1], using as input the nonperturbative quark propagators obtained from the solution of the gap equation, together with an Ansatz for the fully dressed quark-gluon vertex that preserves gauge invariance [31]; and (ii) adding the result computed in (i) to the quenched gluon propagator obtained in the large-volume lattice simulations mentioned above [7]. The key assumption of the method employed is that the effects of a small number of quark families to the gluon propagator may be considered as a ''perturbation'' to the quenched case and that the diagram (a_{11}) constitutes the leading correction. The subleading corrections stem from the (originally) pure Yang–Mills diagrams [graphs (a_1)–(a_{10}) in Fig. 1], which now get modified from the quark loops nested inside them (see Fig. 3 below); their proper inclusion, however, lies beyond our present calculation powers. So, our operating assumption is that these latter effects are small compared to those originating from graph (a_{11}) and will be neglected at this

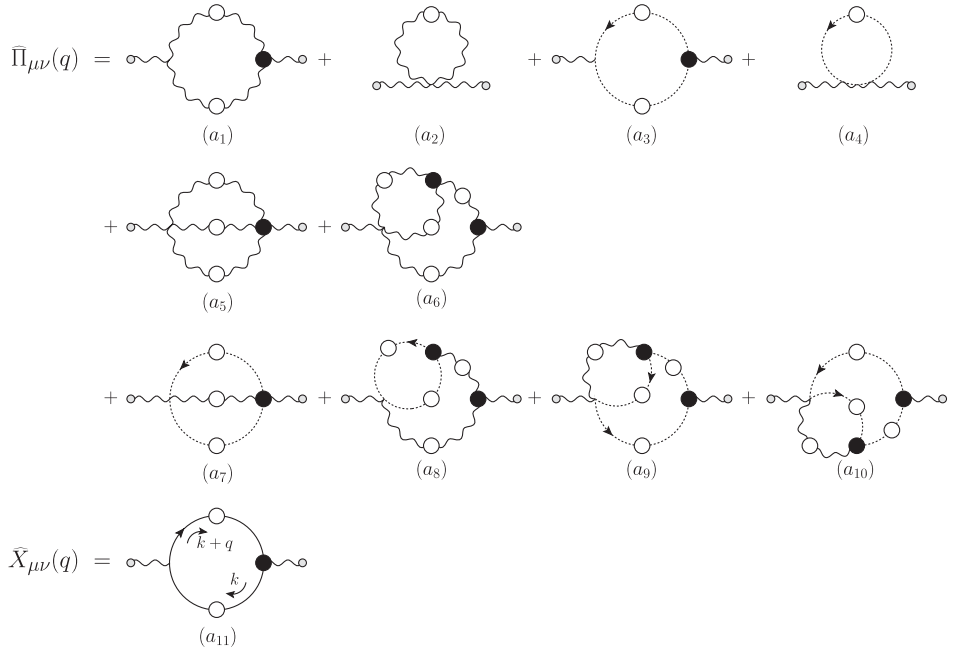

FIG. 1. The full PT-BFM gluon self-energy. White (respectively, black) blobs represents connected (respectively, 1-particle irreducible) Green's functions; the small gray circles on the external legs indicate background gluons.

level of approximation. It is interesting to note that in the context of the "scaling" solutions this latter assumption appears to be indeed reasonable [38,39].

This assumption becomes relevant when implementing point (ii), where the contributions from graphs (a_1)–(a_{10}) will be taken to be exactly the same as those of the quenched case *even when dynamical quarks are present*, thus identifying with the quenched lattice propagator everything except graph (a_{11}). Of course, as is typical in the SDE studies, the validity of this central assumption may be tested only *a posteriori*, either by means of additional, more complicated computations or, more pragmatically, through the levels of agreement achieved with available lattice results. As we will see in the main body of the article [Sec. IV D], the general features emerging from our calculations are consistent with the lattice results of [5,6].

The general framework we will adopt is based on the synthesis of the pinch technique (PT) [16,40–43] with the background field method (BFM) [44], known in the literature as the PT-BFM scheme [13,14,45]. As has been explained in detail in various works, the PT-BFM Green's functions satisfy Abelian-like Ward identities (WIs), instead of the typical Slavnov–Taylor identities (STIs), valid within the linear covariant (R_ξ) gauges [16,44]. The main consequence of this property is that the resulting SDE for the gluon self-energy may be suitably truncated, without compromising the transversality of the answer [13,14,45].

For the case at hand, the new ingredient is the nonperturbative quark loop, which is transverse in the PT-BFM scheme as well as in the R_ξ gauges; thus, at first sight, it would seem that there is no real advantage in using the former scheme. However, the important issue at this point is the exact way this transversality is realized in both cases. In particular, the fact that the fully dressed quark-gluon vertex of the PT-BFM (denoted by $\hat{\Gamma}_\mu$) satisfies a QED-like WI provides a definite advantage over the corresponding conventional vertex (denoted by Γ_μ), which satisfies the STI that involves the quark-ghost scattering kernel [46], a relatively unexplored quantity [see Eqs. (3.3) and (3.4), respectively] [31]. The reason this constitutes an advantage has to do with the fact that, according to the common practice, one must eventually introduce a suitable nonperturbative Ansatz for the full quark-gluon vertex, such that the corresponding WIs (or STIs) are automatically satisfied. The fact that the PT-BFM vertex satisfies a WI instead of an STI simplifies the problem considerably, because it allows one to employ the time-honored Abelian Ansätze existing in the literature [47,48].

The necessary transition from the PT-BFM to the conventional gluon propagator, which is the one simulated on the lattice, is accomplished by means of a special Green's function, usually denoted by G in the literature [14,45]. In the Landau gauge, G is known to coincide with the "Kugo-Ojima" function and to be related to the ghost dressing function by means of a powerful identity enforced by the underlying Becchi–Rouet–Stora–Tyutin (BRST) symmetry [49,50]. Thus, the use of the PT-BFM scheme eliminates the need to refer to quantities such as the quark-ghost kernel, at the very modest price of introducing the aforementioned function, which, due to its STI, can be accurately reconstructed from large-volume lattice data on the ghost dressing functions [50,51], or possibly through direct lattice simulations of the Kugo–Ojima function [52].

The main results of our study may be summarized as follows. The basic effect of the quark loop(s) (one or two families with a constituent mass of the order of 300 MeV) is to suppress considerably the gluon propagator in the IR and intermediate momenta regions, while the ultraviolet (UV) tails increase, exactly as expected from the standard renormalization-group analysis. The final saturation point of the unquenched propagator cannot be reliably calculated at present; the apparent tendency is that the inclusion of light quarks makes the gluon propagator saturate at a lower point, which can be translated into having a larger gluon mass. We emphasize that the way the quark loops affects the value of the gluon mass is indirect: the contribution obtained from graph (a_{11}) vanishes at $q^2 = 0$, so it does not change the gluon mass equation formally [53]; however, it does change its solutions, because of the modification that it induces in the intermediate region of the gluon propagator (which enters in the gluon mass equation). A reliable estimate of this gluon mass difference cannot be obtained without resorting to the full gluon mass equation, whose derivation is currently underway. For the purposes of the present work, the IR "saturation point" of the unquenched propagator will be estimated only approximately, through a process of "extrapolation" of the intermediate momenta region toward the deep IR. The dependence of the results on the renormalization point μ is also studied in detail and appears to be consistent with expectations based on general considerations.

In addition, we present a direct comparison between an unquenched gluon propagator and its corresponding "dressing functions," namely, the ones obtained using the method described above with that found on the lattice [5,6]. Note that, because of its very definition, the dressing function is rather insensitive to the exact value of the final saturation point, moderating to some extent the effect of the aforementioned uncertainty. The resulting comparison with the lattice data is rather favorable, as may be seen in Fig. 19 below; in the momentum region of maximum discrepancy the two curves differ by about 18%, being significantly closer everywhere else.

Finally, it is quite interesting to mention that the use of the perturbative result for the quark loop (see the Appendix) gives rise to an effect that is numerically very close to that obtained through the more sophisticated field-theoretic treatment described above, as can be appreciated in the left panel of Fig. 16 below.

The article is organized as follows. In Sec. II we give a detailed presentation of the basic methodology, main ingredients, and central assumptions of the procedure employed for adding quark loops to the gluon propagator. In Sec. III we elaborate on the way the quark loop is computed nonperturbatively. The main points of this section include (i) the particular form(s) of the full quark-gluon vertex employed, (ii) the actual computation of the loop and its behavior at $q^2 = 0$, (iii) the (subtractive) renormalization procedure, and (iv) the transition to the Euclidean space. Section IV contains the main results of the present work. After introducing the lattice ingredients used as input in our basic formulas, we present the unquenched gluon propagator for $SU(3)$, together with the corresponding dressing function, for a small number of light quark families. Further relevant points, such as the dependence of the results on the renormalization point, as well as the effect of "decoupling" of the heavy quarks are also addressed. In addition, a comparison of the resulting gluon propagator with available lattice data [5,6] is presented. Our main conclusions and further open questions are summarized in Sec. V. Finally, some useful formulas related to the perturbative (one-loop) calculation of the quark loop are summarized in the Appendix.

II. ADDING QUARK LOOPS TO THE GLUON PROPAGATOR

To begin with, in the Landau gauge the gluon propagator (quenched or unquenched) assumes the form

$$\begin{aligned} \Delta_{\mu\nu}(q) &= -i\Delta(q^2)P_{\mu\nu}(q); \\ P_{\mu\nu}(q) &= g_{\mu\nu} - \frac{q_\mu q_\nu}{q^2}. \end{aligned} \tag{2.1}$$

Let us now denote by $\Delta_Q(q^2)$ the full gluon propagator in the presence of quark loops, while the corresponding quenched propagator, i.e., the full gluon propagator in the absence of quark loops, will be denoted simply by $\Delta(q^2)$.

In the PT-BFM scheme, $\Delta(q^2)$ satisfies the following SDE [14–16]:

$$\Delta^{-1}(q^2)P^{\mu\nu}(q) = \frac{q^2 P^{\mu\nu}(q) + i\hat{\Pi}^{\mu\nu}(q)}{[1 + G(q^2)]^2}, \tag{2.2}$$

where

$$\hat{\Pi}^{\mu\nu}(q) = \sum_{i=1}^{10} (a_i)^{\mu\nu}, \tag{2.3}$$

and the relevant fully dressed diagrams (a_i) are shown in Fig. 1. All these diagrams contain only fields appearing in the pure gauge Yang–Mills Lagrangian, namely, gluons and ghosts. The function G appearing in (2.2) is particular to the PT-BFM formalism [14,45]; specifically, it is the form factor associated with the metric tensor $g_{\mu\nu}$ in the Lorentz decomposition of the auxiliary two-point function $\Lambda_{\mu\nu}$, given by [16]

$$\begin{aligned} \Lambda_{\mu\nu}(q) &= -ig^2 C_A \int_k \Delta^\sigma_\mu(k) D(q-k) H_{\nu\sigma}(-q, q-k, k) \\ &= g_{\mu\nu} G(q^2) + \frac{q_\mu q_\nu}{q^2} L(q^2). \end{aligned} \tag{2.4}$$

In the formula above, C_A is the Casimir eigenvalue in the adjoint representation [$C_A = N$ for $SU(N)$], and the d-dimensional integral (in dimensional regularization) is defined according to

$$\int_k \equiv \frac{\mu^\epsilon}{(2\pi)^d}\int \mathrm{d}^d k, \tag{2.5}$$

with $d = 4 - \epsilon$ and μ the 't Hooft mass. The function $\Lambda_{\mu\nu}(q)$, together with the auxiliary function $H_{\mu\nu}(q, p, r)$, is diagrammatically represented in Fig. 2.

Notice that $H_{\mu\nu}$ is related to the (conventional) gluon-ghost Γ^c_μ vertex by the identity

$$p^\nu H_{\nu\mu}(p, r, q) + \Gamma^c_\mu(r, q, p) = 0, \tag{2.6}$$

and that, in the (background) Landau gauge, the following all-order relation holds [49,50]:

$$F^{-1}(q^2) = 1 + G(q^2) + L(q^2). \tag{2.7}$$

The unquenched propagator in the presence of a single quark loop will satisfy an appropriately modified version of (2.2), namely,

$$\Delta_Q^{-1}(q^2)P^{\mu\nu}(q) = \frac{q^2 P^{\mu\nu}(q) + i\hat{\Pi}_Q^{\mu\nu}(q) + i\hat{X}^{\mu\nu}(q)}{[1 + G_Q(q^2)]^2}. \tag{2.8}$$

The main difference between (2.2) and (2.8) is the explicit appearance of $\hat{X}^{\mu\nu}(q)$ on the right-hand side (rhs), originating entirely from diagram (a_{11}) (see again Fig. 1); the closed expression of $\hat{X}^{\mu\nu}(q)$ is given in Eq. (3.11), but is not needed for the qualitative discussion that follows. Specifically, notice that there will be a nonlinear propagation of the changes induced due to $\hat{X}^{\mu\nu}(q)$, which will also affect the original subset of purely Yang–Mills graphs, namely, (a_1)–(a_{10}), given that now the various Green's functions appearing inside them will have been modified by $\hat{X}^{\mu\nu}(q)$. For example, at the "one-loop dressed" level, diagram (a_1) receives quark-loop contributions, such as those shown in Fig. 3, and the same happens with all other graphs belonging to the set (a_1)–(a_{10}). This complicated nonlinear effect is indicated by introducing the subscript Q in the associated self-energy, $\hat{\Pi}_Q^{\mu\nu}(q)$. The quantity $G(q)$ will be similarly affected by the inclusion of the quark loop, as indicated in (2.8) through the substitution

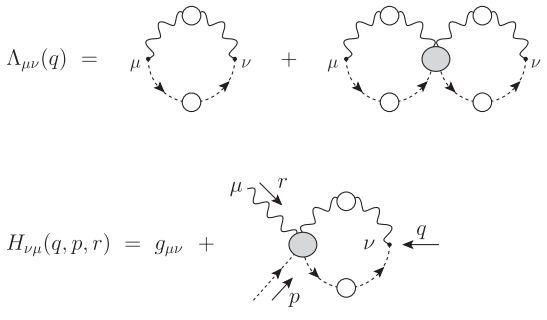

FIG. 2. Definitions and conventions of the auxiliary functions Λ and H. The color and gauge coupling dependence for the field combination shown, $c^a(p)A^b_\mu(r)A^{*c}_\nu(q)$, is gf^{acb}. Gray blobs denote one-particle irreducible (with respect to vertical cuts) Schwinger–Dyson kernels.

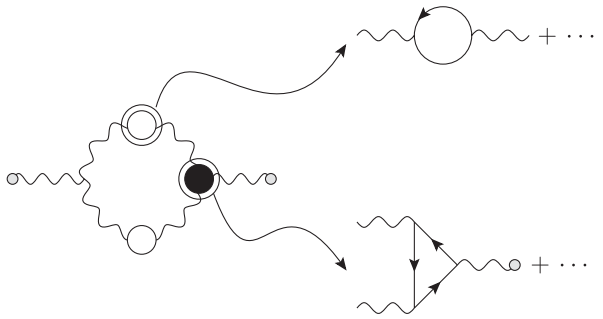

FIG. 3. The nonlinear propagation of the effect of unquenching the gluon propagator through the addition of dynamical fermions, shown here for the one-loop dressed gluon diagram (a_1). Both the internal gluon propagator and the three-gluon vertex get modified (shown here by two representative graphs only); similar modifications occur for all other diagrams.

$G(q) \to G_Q(q)$. In the case of including various quark loops, corresponding to different quark flavors, Q_i, the term $\hat{X}^{\mu\nu}(q)$ in (2.8) is replaced simply by the sum over all quark loops, i.e.,

$$\hat{X}^{\mu\nu}(q) \to \sum_i \hat{X}_i^{\mu\nu}(q). \tag{2.9}$$

The tensorial structure in Eqs. (2.2) and (2.8) may be easily eliminated, by appealing to the transversality properties of the quantities involved on the rhs, namely,

$$q_\mu \hat{\Pi}^{\mu\nu}(q) = 0; \qquad q_\mu \hat{X}^{\mu\nu}(q) = 0; \qquad q_\mu \hat{\Pi}_Q^{\mu\nu}(q) = 0. \tag{2.10}$$

Let us now define the scalar cofactors of these quantities as

$$\begin{aligned} \hat{\Pi}^{\mu\nu}(q) &= P^{\mu\nu}(q)\hat{\Pi}(q^2); \\ \hat{X}^{\mu\nu}(q) &= P^{\mu\nu}(q)\hat{X}(q^2); \\ \hat{\Pi}_Q^{\mu\nu}(q) &= P^{\mu\nu}(q)\hat{\Pi}_Q(q^2). \end{aligned} \tag{2.11}$$

Then, Eqs. (2.2) and (2.8) can be converted to their scalar versions, namely,

$$\Delta^{-1}(q^2) = \frac{q^2 + i\hat{\Pi}(q^2)}{[1 + G(q^2)]^2} \tag{2.12}$$

and

$$\Delta_Q^{-1}(q^2) = \frac{q^2 + i\hat{\Pi}_Q(q^2) + i\hat{X}(q^2)}{[1 + G_Q(q^2)]^2}. \tag{2.13}$$

Equation (2.13) can then be straightforwardly adjusted to include the case of various quark loops, simply by replacing $\hat{X}(q) \to \sum_i \hat{X}_{Q_i}(q)$.

To be sure, the total effect of including quark loops cannot be exactly computed at the level of the SDE, because that would entail the full numerical treatment of the entire series, a task that is beyond our present powers. The way we will proceed instead is the following. We will

use the quenched propagator as our reference, and we will estimate the modifications introduced to it by the presence of the quark loop(s), under certain simplifying assumptions that we will now explain.

To that end, let us cast the quenched gluon propagator $\Delta(q^2)$ into the standard form employed in the recent literature [53–55], which incorporates the crucial feature of IR finiteness, implemented by the presence of a dynamically generated gluon mass; specifically, we set (in Minkowski space)

$$\Delta^{-1}(q^2) = q^2 J(q^2) - m^2(q^2). \tag{2.14}$$

The first term on the rhs of (2.14) corresponds to the "kinetic term," or "wave function" contribution, whereas the second is the momentum-dependent mass (which is positive definite in Euclidean space) [53–55]. As $q^2 \to 0$, we have that $q^2 J_m(q^2) \to 0$; on the other hand, $m^2(0) \neq 0$, and as a result, the gluon propagator is IR finite, $\Delta^{-1}(0) \neq 0$. The exact determination of the components $J(q^2)$ and $m^2(q^2)$ in terms of the quantities appearing on the rhs of (2.2) and (2.8) is a complicated task, leading eventually to a set of intricate coupled integral equations. This exercise has been carried out partially, within the one-loop truncated version of the SDE, considering only the corresponding subset of gluonic contributions [i.e., diagrams (a_1) and (a_2)] [53].

In what follows we will operate under the reasonable assumption that the IR finiteness of the gluon propagator persists in the presence of a relatively small number of quark loops. In other words, we assume that the inclusion of two light quark flavors (up and down type quarks, with constituent masses of about 300 MeV) will affect but not completely destabilize the mechanism responsible for the generation of a dynamical gluon mass, and that their effect may be considered as a perturbation to the quenched case. In the realistic case of QCD, the inclusion of loops containing the remaining heavier quarks is expected to give rise to numerically suppressed contributions (compared to those coming from the light quark loops), consistent with the notion of decoupling; this expectation is in fact clearly confirmed in the results presented in Sec. IV (see, in particular, Fig. 16 below). Instead, the theoretical possibility of increasing the number of loops containing light flavors may lead to effects that can no longer be considered as a perturbation of the quenched case: ten families of light quarks, for example, could alter severely the qualitative behavior of the theory, and as a result, the quenched propagator may have little to do with the unquenched one (for a general discussion on how the IR and UV properties of Yang–Mills theories may be distorted, depending on the number of quark families, see, e.g., [56,57], and references therein).

Thus, under the aforementioned assumptions, Eq. (2.14) will be extended to the case of $\Delta_Q(q^2)$, namely,

$$\Delta_Q^{-1}(q^2) = q^2 J_Q(q^2) - m_Q^2(q^2), \tag{2.15}$$

where the subscript Q in the dynamical gluon mass indicates the possible modifications to $m^2(q^2)$ induced by the quark loop(s), as alluded above. It is important to emphasize that $m^2(q^2)$ will change, despite the fact that the main additional ingredient that distinguishes (2.12) and (2.13), namely, $\hat{X}(q)$, does not contribute at $q^2 = 0$, since $\hat{X}(0) = 0$ [see Eq. (3.19)], and therefore it does not affect *directly* the gluon mass equation [53]; instead, the modification induced is *indirect*, due to the change in the overall shape of $\Delta(q^2)$ throughout the entire range of momenta. In order to gain a qualitative understanding of this last statement, let us consider the IR limit of the approximate gluon mass equation obtained in [53], where only the one-loop dressed graphs (a_1) and (a_2) are considered; in Euclidean space,

$$m^2(0) = -\frac{3C_A}{8\pi}\alpha_s F(0)\int_0^\infty dy m^2(y)[\mathcal{Z}^2(y)]' + \ldots, \tag{2.16}$$

where $\alpha_s = g^2/4\pi$, the prime indicates differentiation with respect to $y = k^2$, and $\mathcal{Z}(y)$ is the "dressing function" of the gluon propagator, defined as

$$\mathcal{Z}(q^2) \equiv q^2\Delta(q^2). \tag{2.17}$$

Evidently, $\mathcal{Z}(0) = 0$. Finally, the ellipses on the rhs of Eq. (2.16) denote contributions from "two-loop dressed" diagrams that have yet to be worked out.

Now, in the presence of quark loops, Eq. (2.16) maintains its functional form, since, as mentioned above, $\hat{X}(0) = 0$; however, the various quantities appearing on its rhs [most notably $\mathcal{Z}(y)$] will be modified, therefore acquiring a subscript "Q" [e.g., $\mathcal{Z}(y) \to \mathcal{Z}_Q(y)$]. As a consequence, the resulting solution gets modified, and we have $m^2(q^2) \to m_Q^2(q^2)$; in what follows we will denote by

$$\lambda^2 \equiv m_Q^2(0) - m^2(0) \tag{2.18}$$

the gluon mass difference at $q^2 = 0$.

As already explained, a solid first-principle determination of λ^2 is not possible at the moment, mainly due to the fact that the available gluon mass Eq. (2.16) is incomplete, since it has been derived from only one subset of the relevant graphs [53]. Therefore, in the analysis presented we will restrict ourselves to extracting an approximate range for λ^2, through the extrapolation of the curves obtained from intermediate momenta toward the deep IR.

In order to estimate the effect of the quark loop(s) on the gluon propagator, we will assume that the main bulk of the correction to the "kinetic" part, $q^2 J_Q(q^2)$, is due to the direct presence of the extra diagram (a_{11}). Instead, the nonlinear effect due to the fact that the graphs (a_1)–(a_{10}) develop an indirect quark dependence, i.e., $\hat{\Pi}(q^2) \to \hat{\Pi}_Q(q^2)$, is predominantly responsible for the change in the gluon mass, as captured in (2.18), inducing minor changes to the kinetic part $q^2 J_Q(q^2)$. Finally, we will approximate the function $G_Q(q^2)$ appearing in the denominator of Eq. (2.13) by the quenched expression, i.e., $G_Q(q^2) \to G(q^2)$; as can be seen from its defining equation Eq. (2.4) and Fig. 2, quark loops enter

only as "higher order" effects, according to our general philosophy, and their effect should be small.

Thus, within this approximation scheme, the quantity $J_Q(q^2)$ will be given by

$$q^2 J_Q(q^2) = q^2 J(q^2) + \frac{i\hat{X}(q^2)}{[1+G(q^2)]^2}. \tag{2.19}$$

If we now combine Eqs. (2.14), (2.15), (2.16), and (2.18), it is easy to arrive at the result (Minkowski space)

$$\Delta_Q(q^2) = \frac{\Delta(q^2)}{1+\{i\hat{X}(q^2)[1+G(q^2)]^{-2} - \lambda^2\}\Delta(q^2)}. \tag{2.20}$$

In what follows we will identify the quenched propagator $\Delta(q^2)$ appearing on the rhs of (2.20) with the one obtained from the large-volume lattice simulations [7], to be denoted by $\Delta_L(q^2)$. So, effectively one assumes that $\Delta_L(q^2)$ is a solution of the full SDE equation, with no quarks, given in (2.12); thus, when using (2.20) we will be carrying out the replacement $\Delta(q^2) \to \Delta_L(q^2)$.

The rationale behind this choice lies in the fact that even though the (one-loop dressed) truncated PT-BFM SDE for the gluon two-point function reproduces qualitatively the lattice results [15], it underestimates the propagator size in the intermediate momentum region, as can clearly be seen in Fig. 4. This quantitative discrepancy would seem to indicate that there are sizable contributions from the two-loop dressed diagrams left out in the analysis of [15]; although their incorporation in the SDE is in principle feasible, the technical challenges that must be faced are highly nontrivial, since it would involve among other things modeling the full four-gluon vertex, a practically unexplored quantity.

The net effect of the aforementioned discrepancy is that when the gluon propagator SDE result is used as an input inside the quark-gap equation, one cannot get realistic quark propagators and consequently reliable estimates for the quark-loop $\hat{X}(q^2)$ where these propagators explicitly enter. On the other hand, by using the lattice results for the gluon propagator, one achieves a chiral symmetry breaking pattern that provides for dynamically generated quark masses compatible with phenomenology [31], thusly ensuring the self-consistency of the whole scheme.

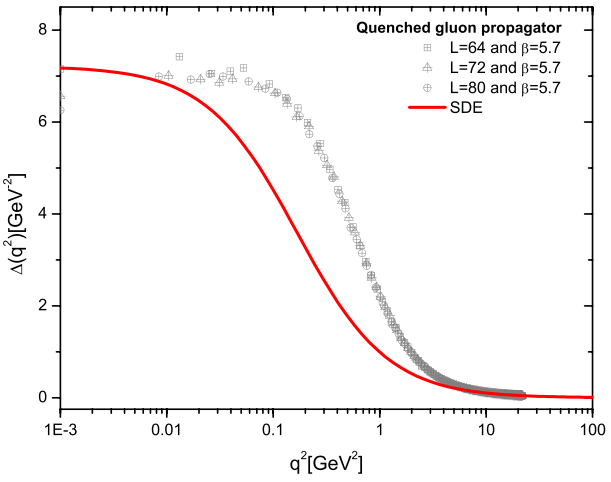

FIG. 4 (color online). Comparison between the gluon propagator, $\Delta(q^2)$, obtained from the SDE renormalized at $\mu = 4.3$ GeV (solid red curve) and the lattice data (gray symbols) of Ref. [7].

III. NONPERTURBATIVE QUARK LOOP IN THE PT-BFM SCHEME

In this section we present the actual nonperturbative calculation of the quark-loop diagram (a_{11}), finally expressing the answer exclusively in terms of the functions $A(p)$ and $B(p)$, appearing in the Dirac decomposition of the full quark propagator [see (3.7)]. The calculation relies on the use of suitable Ansätze for the fully dressed quark-gluon vertex appearing in (a_{11}), presented and discussed in the corresponding subsection. The Euclidean version of the (renormalized) master formula that we use in the next section in order to estimate the effect of the quark loop on the gluon propagator is given in Eq. (3.57).

A. The quark-gluon vertex

The quantity responsible for the difference between the quark loop in the conventional covariant gauges and the PT-BFM scheme is the fully dressed quark-gluon vertex. Specifically, let us denote the fully dressed PT-BFM quark-gluon vertex by $\hat{\Gamma}^a_\mu$ and factor out the color structure, according to

$$\hat{\Gamma}^{\,a}_{\mu}(p_1, p_2, p_3) = g t^a \hat{\Gamma}_\mu(p_1, p_2, p_3), \tag{3.1}$$

where all momenta p_i enter (see Fig. 5); at tree-level, $\hat{\Gamma}^{(0)}_\mu = \gamma_\mu$. In the equation above, t^a represents the N^2-1 Hermitian and traceless generators of the $SU(N)$ gauge group, satisfying the algebra

$$[t^a, t^b] = i f^{abc} t^c, \tag{3.2}$$

with f^{abc} the totally antisymmetric group structure constants. In the $SU(3)$ case, with the quarks in the fundamental

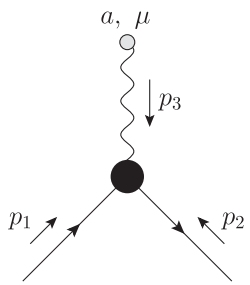

FIG. 5. The full PT-BFM quark-gluon vertex $\hat{\Gamma}^a_\mu$. Note that $p_1 \leftrightarrow p_2$ with respect to the conventions used in [31,72].

representation, $t^a = \lambda^a/2$, where λ^a are the Gell–Mann matrices.

In the conventional formulation within the linear covariant gauges, the quark-gluon vertex, to be denoted by $\Gamma_\mu(p_1, p_2, p_3)$, satisfies the well-known STI [46]

$$ip_3^\mu \Gamma_\mu(p_1, p_2, p_3) = F(p_3)[S^{-1}(p_1)H(p_2, p_1, p_3) - \bar{H}(p_1, p_2, p_3)S^{-1}(-p_2)], \quad (3.3)$$

where $S^{-1}(p)$ is the inverse of the full quark propagator, $H(p_2, p_1, p_3)$ is the quark-ghost scattering kernel diagrammatically defined in Fig. 6, and $\bar{H}(p_1, p_2, p_3)$ is its "conjugate."

In contrast, in the PT-BFM scheme, the vertex $\hat{\Gamma}_\mu$ satisfies the QED-like WI [16,44]

$$ip_3^\mu \hat{\Gamma}_\mu(p_1, p_2, p_3) = S^{-1}(p_1) - S^{-1}(-p_2), \quad (3.4)$$

with no reference whatsoever to the ghost sector. Then, the most general Ansatz for the longitudinal part of $\hat{\Gamma}_\mu$ that satisfies (3.4) is given by [47]

$$\hat{\Gamma}_\mu(p_1, p_2, p_3) = L_1(p_1, p_2)\gamma_\mu + L_2(p_1, p_2)(\not{p}_1 - \not{p}_2)(p_1 - p_2)_\mu + L_3(p_1, p_2)(p_1 - p_2)_\mu. \quad (3.5)$$

The form factors L_i appearing in the expression above are given by

$$L_1(p_1, p_2) = \frac{A(p_1) + A(p_2)}{2}; \quad L_2(p_1, p_2) = \frac{A(p_1) - A(p_2)}{2(p_1^2 - p_2^2)}; \quad L_3(p_1, p_2) = -\frac{B(p_1) - B(p_2)}{p_1^2 - p_2^2}, \quad (3.6)$$

where the functions $A(p)$ and $B(p)$ are defined as

$$S^{-1}(p) = -i[A(p)\not{p} - B(p)] = -iA(p)[\not{p} - \mathcal{M}(p)], \quad (3.7)$$

and the ratio $\mathcal{M}(p) = B(p)/A(p)$ is the dynamical quark mass function. For later convenience, we will denote the dynamical quark mass function at $p^2 = 0$ by $\mathcal{M}(0) \equiv M$. Therefore, at tree level ($A = 1$, $B = M$), and one has $L_1 = 1$ and $L_2 = L_3 = 0$. The resulting vertex reads

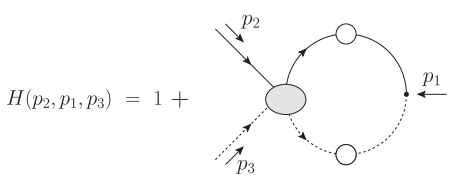

FIG. 6. Diagrammatic representation of the quark-ghost scattering kernel $H(p_1, p_2, p_3)$.

$$\hat{\Gamma}^\mu(p_1, p_2, p_3) = \frac{A(p_1) + A(p_2)}{2}\gamma^\mu + \frac{(p_1 - p_2)^\mu}{p_1^2 - p_2^2} \times \left\{[A(p_1) - A(p_2)]\frac{\not{p}_1 - \not{p}_2}{2} + [B(p_1) - B(p_2)]\right\} \quad (3.8)$$

and is known in the literature as the Ball–Chiu (BC) vertex [47].

We emphasize that in the context of the PT-BFM the *longitudinal* part of the above vertex is complete, as far as the WI it satisfies is concerned. Indeed, the expression in (3.8) satisfies the *exact* WI that $\hat{\Gamma}_\mu$ is supposed to obey, namely, (3.4). As is well known, the BC vertex has been employed extensively in the literature (especially in studies of chiral symmetry breaking) [58] as an approximate (denominated "abelianized") version of the conventional Γ_μ defined in the covariant gauges. Indeed, the fully dressed quark-gluon vertex entering into the quark-gap equation is Γ_μ and not $\hat{\Gamma}_\mu$, for the simple reason that the corresponding gluon is quantum and not background; indeed, the gluon in the quark-gap equation is internal (i.e., it is irrigated by the virtual momenta), in contrast to the gluon of the quark loop, which is external (carries physical momentum). Therefore, use of the expression given in (3.8) into the quark-gap equation constitutes only an approximation, since it fails to satisfy the full STI (3.3) that Γ_μ should obey, unless the corresponding ghost sector is turned off.

Note that the BC vertex has been generalized accordingly in [31], in order to fulfill the exact STI (3.3), thus justifying its use inside the quark-gap equation. The corresponding L_i are considerably more complicated than those given in (3.6), involving the ghost dressing function F and the various form factors of the quark-ghost kernel $H(p_1, p_2, p_3)$ [31]. In fact, an additional fourth form factor, L_4, makes its appearance in the Lorentz expansion corresponding to (3.5), multiplying $\sigma_{\mu\nu} = i/2[\gamma_\mu, \gamma_\nu]$; it is then easy to verify that this latter, genuinely non-Abelian vertex of [31] reduces to that of (3.8) in the limit of a trivial ghost sector, i.e., by setting $F(p) = 1$ and $H = 1$.

Finally, let us comment on an alternative form of the quark-gluon vertex $\hat{\Gamma}_\mu(p_1, p_2, p_3)$, known in the literature as the Curtis and Pennington (CP) vertex [48], to be denoted by $\hat{\Gamma}_\mu^{\rm CP}$. This latter vertex satisfies also the WI of (3.4) and differs from the vertex of (3.8) by a transverse (automatically conserved) contribution, which improves its properties under multiplicative renormalizability. Specifically,

$$\hat{\Gamma}_\mu^{\rm CP}(p_1, p_2, p_3) = \hat{\Gamma}_\mu(p_1, p_2, p_3) + [\gamma_\mu(p_2^2 - p_1^2) + (p_2 - p_1)_\mu \not{p}_3]\hat{\Gamma}_{\rm T}(p_1, p_2, p_3), \quad (3.9)$$

where

$$\hat{\Gamma}_{\rm T}(p_1, p_2, p_3) = \frac{[A(p_2) - A(p_1)](p_1^2 + p_2^2)}{2\{(p_2^2 - p_1^2)^2 + [\mathcal{M}^2(p_2) + \mathcal{M}^2(p_1)]^2\}}. \tag{3.10}$$

In the analysis that follows we will use both the BC and the CP vertices, and compare the difference they induce to the various quantities of interest.

B. The quark loop

Let us now turn to the quark-loop diagram (a_{11}) of the PT-BFM scheme. Factoring out the trivial color structure δ^{ab}, we obtain

$$\hat{X}^{\mu\nu}(q^2) = -g^2 d_f \int_k {\rm Tr}[\gamma^\mu S(k)\hat{\Gamma}^\nu(k+q,-k,-q)S(k+q)], \tag{3.11}$$

where d_f is the Dynkin index of the fundamental representation [$d_f = 1/2$ for $SU(3)$].

Since by virtue of the WI (3.4) the quark loop $\hat{X}^{\mu\nu}(q^2)$ is transverse,[1]

$$q_\mu \hat{X}^{\mu\nu}(q^2) = 0, \tag{3.12}$$

we have that $\hat{X}^{\mu\nu}(q^2) = \hat{X}(q^2)P^{\mu\nu}(q)$, as anticipated in Eq. (2.11). Then, contracting with $g_{\mu\nu}$, and setting $d_f = 1/2$, we obtain

$$\hat{X}(q^2) = -\frac{g^2}{2(d-1)} \times \int_k {\rm Tr}[\gamma^\mu S(k)\hat{\Gamma}_\mu(k+q,-k,-q)S(k+q)]. \tag{3.13}$$

After inserting the full vertex (3.5) into (3.13) and taking the trace, we find one term for each of the form factors L_i. Specifically, we have that

$$\hat{X}(q^2) = -\frac{2g^2}{d-1}\int_k \frac{1}{A_a A_b (k^2 - \mathcal{M}_a^2)[(k+q)^2 - \mathcal{M}_b^2]} \times \sum_{i=1}^{3} T_i(k, k+q), \tag{3.14}$$

where the subindex "a" (respectively, "b") indicates that the corresponding function is evaluated at momentum k (respectively, $k+q$), with

$$\begin{aligned} T_1(k,k+q) &= L_1\{(2-d)(k^2 + k\cdot q) + d\mathcal{M}_a\mathcal{M}_b\},\\ T_2(k,k+q) &= L_2\{2[k\cdot(2k+q)][(k+q)\cdot(2k+q)] \\ &\quad - k\cdot(k+q)(2k+q)^2 + (2k+q)^2\mathcal{M}_a\mathcal{M}_b\},\\ T_3(k,k+q) &= L_3\{\mathcal{M}_b[(2k+q)\cdot k] \\ &\quad + \mathcal{M}_a[(2k+q)\cdot(k+q)]\}. \end{aligned} \tag{3.15}$$

Before studying in detail each term, let us consider $\hat{X}(q^2)$ in the limit $q \to 0$. Using the expressions given in Eq. (3.6), and dropping the subindices (all quantities being evaluated at k now), one finds

$$\hat{X}(0) = -\frac{2g^2}{d-1}\int_k \frac{1}{A^2(k^2 - \mathcal{M}^2)^2}\{A[(2-d)k^2 + d\mathcal{M}^2] + 2A'k^2(k^2 + \mathcal{M}^2) - 4k^2B'\mathcal{M}\}. \tag{3.16}$$

The important point to recognize now is that the integral on the rhs of (3.16) vanishes by virtue of an identity valid in dimensional regularization. This identity, referred to as the "seagull identity" in the recent literature [54] constitutes the generalization of the simple identity (A3) employed in the Appendix for the one-loop perturbative result.

Specifically, the seagull identity reads

$$\int_k k^2 f'(k^2) + \frac{d}{2}\int_k f(k^2) = 0, \tag{3.17}$$

where the "prime" denotes differentiation with respect to k^2, i.e., $f'(k^2) \equiv \frac{{\rm d}f(k^2)}{{\rm d}k^2}$. Interestingly enough, using inside Eq. (3.17) the function

$$f(k^2) = [A(k^2)(k^2 - \mathcal{M}^2(k^2))]^{-1}, \tag{3.18}$$

namely, the all-order generalization of the one-loop $(k^2 - M^2)^{-1}$ employed in Eq. (A3), one obtains precisely the integral on the rhs of (3.16); therefore,

$$\hat{X}(0) = 0, \tag{3.19}$$

as announced.

Let us now compute the quark self-energy $\hat{X}^{CP}(q^2)$ obtained by substituting into (3.11) the vertex $\hat{\Gamma}^\mu_{\rm CP}$, given in (3.9) and (3.10). The answer will be expressed as a deviation from $\hat{X}(q^2)$, namely,

$$\hat{X}^{\rm CP}(q^2) = \hat{X}(q^2) + \delta\hat{X}(q^2), \tag{3.20}$$

where

$$\delta\hat{X}(q^2) = 2g^2\int_k \frac{[\mathcal{M}_a\mathcal{M}_b - (k^2 + k\cdot q)][(k+q)^2 - k^2]}{A_aA_b(k^2 - \mathcal{M}_a^2)[(k+q)^2 - \mathcal{M}_b^2]}\hat{\Gamma}_{\rm T} \times (k+q, -k, -q). \tag{3.21}$$

It is easy to verify that the integral on the rhs of (3.21) vanishes in the limit $q \to 0$, because, as can be seen

[1]Note that the corresponding quark-loop in the covariant gauges, i.e., with $\hat{\Gamma}^\nu \to \Gamma^\nu$ is also transverse, by virtue of the STI (3.3).

directly from (3.10), $\hat{\Gamma}_{\rm T}(p_1, -p_1, 0) = 0$. Therefore, the property of (3.16) persists, namely, $\hat{X}^{\rm CP}(0) = 0$.

C. Renormalization I

Up until this point we have worked with unrenormalized quantities. The next step is to renormalize the basic formulas obtained above, and, in particular, the full gluon propagator of Eq. (2.20) and the quark contributions $\hat{X}(q^2)$ [and $\hat{X}^{\rm CP}(q^2)$], within a self-consistent renormalization scheme, namely, a scheme that respects the underlying gauge symmetry, as captured by the STIs and WIs satisfied by the various Green's functions. It turns out that, for the specific task at hand, the unquenched gluon propagator obtained from the corresponding SDE must be renormalized within the momentum subtraction (MOM) scheme. This choice is dictated by the fact that our final results will be expressed as deviations from the quenched gluon propagator obtained from the lattice, where the latter scheme has been employed [59–61].

In the case of a two-point function, which depends on a single momentum, the MOM condition is unique; however, in the case of higher Green's functions (with more than one momentum), one has in principle a variety of choices of fixed kinematic configurations, where the normalization condition may be imposed. These choices, in turn, define a family of MOM-type schemes and give, correspondingly, rise to different renormalization-group equations [62]. For instance, in the case of a three-point function, one may impose the symmetric condition $p_1^2 = p_2^2 = p_3^2 = \mu^2$ (with $p_1 \cdot p_2 = p_2 \cdot p_3 = p_1 \cdot p_3 = -\mu^2/2$), or the asymmetric choice $p_1^2 = p_2^2 = \mu^2$, and $p_3^2 = 0$, corresponding to the so-called $\widetilde{\rm MOM}$ scheme (for a concrete example; see next section).

Given that several fully dressed vertices enter into the SDE for the gluon propagator, as can be clearly seen in Fig. 1, the exact way of renormalizing them is of paramount theoretical importance. However, given that the *full* implementation of the renormalization program at the level of the SDE is technically far beyond our present powers, some of the subtleties related to the renormalization choice do not manifest themselves, due to a variety of simplifications that the SDE practitioners introduce, as we will now explain in some detail.

The most drastic approximation employed in this context is to carry out a *subtractive* instead of a multiplicative renormalization. To fix the ideas, let us consider a dimensionless two-point function, to be denoted by $f(q^2)$, satisfying an unrenormalized SDE of the schematic form

$$f^{-1}(q^2) = 1 + \int_k K(q, k) f(k^2), \tag{3.22}$$

where the kernel K is composed in general by additional Green's functions, kinematic factors, the coupling constant, etc. Let us assume that $f(q^2)$ is renormalized through the introduction of the cutoff-dependent renormalization constant Z_f, according to the standard relation $f(q^2) = Z_f f_R(q^2)$. Similarly, the kernel K is renormalized by introducing an appropriate renormalization constant Z_K, namely, $K_R(q, k) = Z_K K(q, k)$; of course, Z_K is obtained as a combination of the corresponding renormalization constants that make finite the individual ingredients that build up K, taking into account possible constraints imposed by the WIs or STIs. It is precisely at this point where the renormalization choices for the vertices, as well as a variety of additional subtleties, would make their appearance. Then, defining $Z \equiv Z_f Z_K$, Eq. (3.22) becomes

$$f_R^{-1}(q^2) = Z_f + Z \int_k K_R(q, k) f_R(k^2). \tag{3.23}$$

As is well known [63], the presence of Z in front of the integral enforces the cancellation of the overlapping divergences. Of course, the exact realization of these cancellations hinges on the precise form of $K_R(q, k)$; given that the latter is almost invariably determined under certain approximations (such as, for example, the use of an Ansatz for some of its ingredients, e.g., the quark-gluon vertex in our case), one ends up mishandling these overlapping divergences. Given this limitation, it is customary to simplify the analysis further by setting $Z = 1$; at this stage, all knowledge of the precise properties of the individual renormalization constants making up Z are lost. Note, however, that the information regarding the renormalization procedure employed is not lost, being encoded in the precise closed form of $K_R(q, k)$: for example, $K_R(q, k)$ is different in the MOM and the $\widetilde{\rm MOM}$ schemes.

This last approximation converts the procedure of multiplicative renormalization into subtractive, in the sense that now, the imposition of a renormalization condition, such as $f_R^{-1}(\mu^2) = 1$, determines Z_f as

$$Z_f = 1 - \int_k K_R(\mu, k) f_R(k^2), \tag{3.24}$$

and casts Eq. (3.23) into the form

$$f_R^{-1}(q^2) = 1 + \left[\int_k K_R(q, k) f_R(k^2) - \int_k K_R(\mu, k) f_R(k^2) \right]. \tag{3.25}$$

If we were to introduce a self-energy-like quantity, to be denoted by $h(q^2)$, such that $f^{-1}(q^2) = 1 + h(q^2)$, then from Eq. (3.22) we have

$$h(q^2) = \int_k K(q, k) f(k^2), \tag{3.26}$$

and so, since $f_R^{-1}(q^2) = 1 + h_R(q^2)$, Eq. (3.25) reduces to

$$h_R(q^2) = h(q^2) - h(\mu^2), \tag{3.27}$$

with the MOM condition $h_R(\mu^2) = 0$ built in. Thus, the subtractive renormalization procedure finally amounts to

$$Z_f f^{-1}(q^2) = f_R^{-1}(q^2) = 1 + h_R(q^2) = 1 + [h(q^2) - h(\mu^2)]. \tag{3.28}$$

If $f(q^2)$ has dimensions of $[m]^{-2}$, the original SDE in Eq. (3.22) is modified by replacing $1 \to q^2$ on its rhs, and the corresponding renormalization condition is $f_R^{-1}(\mu^2) = \mu^2$; thus, Eq. (3.25) becomes

$$f_R^{-1}(q^2) = q^2 + \left[\int_k K_R(q,k) f_R(k^2) - \frac{q^2}{\mu^2}\int_k K_R(\mu,k) f_R(k^2)\right]. \tag{3.29}$$

If we set $f^{-1}(q^2) = q^2 + H(q^2)$, then Eq. (3.29) yields

$$H_R(q^2) = \left[\int_k K_R(q,k) f_R(k^2) - \frac{q^2}{\mu^2}\int_k K_R(\mu,k) f_R(k^2)\right] = H(q^2) - \frac{q^2}{\mu^2} H(\mu^2). \tag{3.30}$$

Evidently, $H_R(\mu^2) = 0$, as it should. In what follows we will make use of both the dimensionless and dimensionful procedures, given that $G(q^2)$ is dimensionless, while the gluon propagator is dimensionful.

The detailed application of this general methodology to the case at hand proceeds by introducing the appropriate renormalization relations for all relevant fields and Green's functions. Let us first describe the renormalization of the quenched part of the SDE, involving graphs (a_1)–(a_{10}), but not (a_{11}). The starting point is Eq. (2.12), and the basic renormalization relations employed are

$$\Delta_R(q^2) = Z_A^{-1}\Delta(q^2),$$
$$1 + G_R(q^2) + L_R(q^2) = Z_\Lambda[1 + G(q^2) + L(q^2)]. \tag{3.31}$$

Now, as is well known [50,51], the validity of the BRST-driven relation Eq. (2.7) before and after renormalization imposes the restriction $Z_\Lambda = Z_c$, where Z_c is the ghost renormalization constant, i.e., $F_R(q^2) = Z_c^{-1} F(q^2)$. In addition, Eq. (2.7) prevents $G(\mu^2)$ from vanishing when, according to the MOM prescription, $F(\mu^2) = 1$; instead, we must impose that $G(\mu^2) = -L(\mu^2)$. However, given that $L(x)$ is considerably smaller than $G(x)$ in the entire range of momenta, we can use the approximation $1 + G(\mu^2) \approx F^{-1}(\mu^2) = 1$, without introducing an appreciable numerical error [50,51]. Then, the subtractive renormalization of $G(q^2)$, along the lines presented in Eqs. (3.23), (3.24), (3.25), (3.26), and (3.27), yields

$$G_R(q^2) = G(q^2) - G(\mu^2). \tag{3.32}$$

Next, renormalizing Eq. (2.12) by employing the appropriate renormalization constants, using Eq. (3.32), and introducing $\hat{Z}_A = Z_A Z_c^2$, namely, the wave-function renormalization constant of the PT-BFM propagator [see Eq. (3.63)], we obtain

$$\Delta_R^{-1}(q^2) = \frac{\hat{Z}_A q^2 + i\sum_{i=1}^{10} Z_i a_{i,R}(q^2)}{[1 + G_R(q^2)]^2}. \tag{3.33}$$

The Z_i are the combined renormalization constants corresponding to each graph [the analogues of the Z in Eq. (3.23)]; their precise composition in terms of the renormalization constants of the fundamental fields can be worked out, but is of no interest for our purposes, since, as was done in Eq. (3.23), we will set $Z_i = 1$. Then, imposing the MOM condition $\Delta_R^{-1}(\mu^2) = \mu^2$, we can solve for $\hat{Z}_A$ and cast Eq. (3.33) into the form

$$\Delta_R^{-1}(q^2) = \frac{q^2 + i\sum_{i=1}^{10}[a_{i,R}(q^2) - \frac{q^2}{\mu^2} a_{i,R}(\mu^2)]}{[1 + G_R(q^2)]^2}, \tag{3.34}$$

or, using Eq. (2.3), we have that

$$\Delta_R^{-1}(q^2) = \frac{q^2 + i\hat{\Pi}_R(q^2)}{[1 + G_R(q^2)]^2}, \tag{3.35}$$

with

$$\hat{\Pi}_R(q^2) = \hat{\Pi}(q^2) - \frac{q^2}{\mu^2}\hat{\Pi}(\mu^2). \tag{3.36}$$

We next take a closer look at the renormalization of the quark contributions $\hat{X}(q^2)$; to that end, we must first introduce the following relations:

$$S_R(p) = Z_Q^{-1} S(p),$$
$$\hat{\Gamma}_R^\mu(p_1, p_2, p_3) = Z_1 \Gamma^\mu(p_1, p_2, p_3), \tag{3.37}$$
$$g_R = Z_g^{-1} g.$$

Notice that, by virtue of the WI (3.4), the renormalization constant satisfies the QED-like relations

$$Z_1 = Z_Q; \qquad Z_g^2 = \hat{Z}_A, \tag{3.38}$$

perturbatively (to all orders) as well as nonperturbatively. Within the MOM scheme that we employ, neglecting for simplicity the quark mass, we have that $S^{-1}(p) = A(p)\not{p}$, and it is clear that the MOM normalization condition for the quark wave function is $A_R(\mu) = 1$. Now, since in the Landau gauge the quark self-energy and the quark-gluon vertex are actually finite, the Z_Q that enforces the above condition is a *finite* renormalization constant. However, at higher orders, Z_Q receives infinite (cutoff-dependent) contributions.

Then, one may repeat the procedure employed for the quenched case presented above, simply by adding the contribution (a_{11}) in the sum appearing on the rhs of Eq. (3.33). The corresponding factor Z_{11} may be determined from the expression for $\hat{X}(q^2)$ in Eq. (3.13), together with the relations of Eq. (3.37), taking into account the constant $\hat{Z}_A$ coming from the $(1 + G)^2$ and the Δ^{-1} on the rhs. Specifically, after the use of Eq. (3.38), one obtains that $Z_{11} = Z_Q$. Setting next $Z_Q = 1$, as was done with the rest of the Z_i, one obtains the subtractive renormalization results

$$\Delta^{-1}_{Q,R}(q^2) = \frac{q^2 + i[\hat{\Pi}_{Q,R}(q^2) + \hat{X}_R(q^2)]}{[1 + G_{Q,R}(q^2)]^2}, \tag{3.39}$$

where, as before, $\hat{\Pi}_{Q,R}(q^2) = \hat{\Pi}_Q(q^2) - \frac{q^2}{\mu^2}\hat{\Pi}_Q(\mu^2)$, $G_{Q,R}(q^2) = G_Q(q^2) - G_Q(\mu^2)$, and

$$\hat{X}_R(q^2) = \hat{X}(q^2) - \frac{q^2}{\mu^2}\hat{X}(\mu^2). \tag{3.40}$$

Then, according to the key operating assumption explained in the previous section, the unquenched quantities $\hat{\Pi}_Q(q^2)$ and $G_Q(q^2)$ are to be approximated simply by their quenched counterparts, $\hat{\Pi}(q^2)$ and $G(q^2)$, respectively. Consequently, it is straightforward to verify that the renormalized version of (2.20) is given by

$$\Delta_{Q,R}(q^2) = \frac{\Delta_R(q^2)}{1 + \{i\hat{X}_R(q^2)[1 + G_R(q^2)]^{-2} - \lambda^2\}\Delta_R(q^2)}. \tag{3.41}$$

In this context, the gluon mass related term λ^2 merits, finally, some additional comments. As has been emphasized amply in recent works, the seagull identity of (3.17), when applied to the gluon mass equation, enforces the annihilation of all quadratic divergences [53,54]. This is a point of central importance, because the disposal of such divergences (had they survived) would require the introduction in the original Yang–Mills Lagrangian of a counterterm of the form $m_0^2 A_\mu^2$, which is, however, forbidden by the local gauge invariance, which must remain intact. Therefore, at least in principle, the renormalization of the gluon mass equation proceeds as in the case of the homogeneous quark mass equation (obtained from the corresponding gap equation without a current mass term), simply by renormalizing (multiplicatively) the various quantities appearing on its rhs [53]. Note, however, that these considerations, theoretically important as they may be, are of limited practical relevance for the present work, because, as already mentioned, the quantity λ^2 will be not determined dynamically, but rather fitted from the (extrapolated) solutions obtained.

D. Renormalization II

In the previous subsection we have addressed several issues related to the renormalization procedure, placing special emphasis on the details of the subtractive renormalization, as applied in the context of the SDE analysis. In this subsection we will focus on some additional points pertinent to the particularities of the present work, and especially of the PT-BFM framework that we employ.

Returning to the MOM-inspired family of renormalization schemes, mentioned in general terms in the previous section, it is instructive to gain by means of an explicit (perturbative) example some further insight on how different renormalization-group equations may emerge [62]. To that end, let us consider a generic type of three-particle vertex (all indices suppressed), of the form

$$\Gamma(p_1, p_2, p_3) = 1 + \frac{a}{\epsilon} + \Lambda(p_1, p_2, p_3), \tag{3.42}$$

where we have used dimensional regularization, a is a numerical constant, and the function $\Lambda(p_1, p_2, p_3)$ is finite. Both quantities are of order $\mathcal{O}(g^2)$, and we will neglect terms of order $\mathcal{O}(g^4)$ and higher.

Renormalization proceeds by introducing Z_1 such that the renormalized vertex

$$\Gamma_R(p_1, p_2, p_3) = Z_1\Gamma(p_1, p_2, p_3) \tag{3.43}$$

is finite. Clearly, the normalization choice imposed on $\Gamma_R(p_1, p_2, p_3)$ fixes the constant Z_1. Indeed, let us write Z_1 in the form

$$Z_1 = 1 + \frac{b}{\epsilon} + C, \tag{3.44}$$

where b and C are constants of order $\mathcal{O}(g^2)$. Substituting Eq. (3.44) into Eq. (3.43) and using Eq. (3.42), we see that the requirement of finiteness of Γ_R fixes b (in all schemes) to be $b = -a$; on the other hand, the value of C is scheme dependent. Specifically, after canceling the $1/\epsilon$ terms one has

$$\Gamma_R(p_1, p_2, p_3) = 1 + \Lambda(p_1, p_2, p_3) + C. \tag{3.45}$$

Imposing now the symmetric MOM condition $\Gamma_R(p_1^2 = p_2^2 = p_3^2 = \mu^2) = 1$, we have from Eq. (3.45)

$$C_{\rm MOM} = -\Lambda(p_1^2 = p_2^2 = p_3^2 = \mu^2), \tag{3.46}$$

whereas in the $\widetilde{\rm MOM}$ scheme, where $\Gamma_R(p_1^2 = p_2^2 = \mu^2, p_3^2 = 0) = 1$, we have correspondingly

$$C_{\widetilde{\rm MOM}} = -\Lambda(p_1^2 = p_2^2 = \mu^2, p_3^2 = 0), \tag{3.47}$$

and so Z_1 differs from one MOM scheme to the next.

The scheme dependence exemplified above will eventually reflect itself in the definition of the β function of the theory, and the corresponding running coupling. Specifically, given that the coefficients of the β function are scheme independent up to two loops, in general the scheme dependence related to the various MOM-inspired choices will make its appearance from the third loop and beyond, giving rise to different running couplings [62].

In the analysis presented throughout this article, the MOM scheme employed for the various vertices is the one that corresponds to the symmetric condition: at $p_1^2 = p_2^2 = p_3^2 = \mu^2$ the renormalized vertices collapse to their tree-level values. In fact, interestingly enough, this particular normalization does not constitute a choice, but is instead imposed *a fortiori* by the QED-like WIs characteristic of the PT-BFM framework [16].

In order to appreciate this point, let us return for concreteness to the renormalization of the quark loop, and, in particular, Eqs. (3.37) and (3.38). Once the quark self-energy has been renormalized by Z_Q, the equality $Z_1 = Z_Q$ obliges one to use Z_Q also in the renormalization

of the vertex $\hat{\Gamma}^\mu$. Specifically, neglecting for simplicity the mass terms, the vertex of Eq. (3.8) is renormalized as

$$\begin{aligned}\hat{\Gamma}^\mu_R(p_1,p_2,p_3) &= Z_Q\hat{\Gamma}^\mu(p_1,p_2,p_3)\\ &= Z_Q\Big\{\frac{A(p_1)+A(p_2)}{2}\gamma^\mu+\frac{(p_1-p_2)^\mu}{p_1^2-p_2^2}\\ &\quad\times[A(p_1)-A(p_2)]\Big(\frac{\not{p}_1-\not{p}_2}{2}\Big)\Big\}\\ &= \frac{A_R(p_1)+A_R(p_2)}{2}\gamma^\mu+\frac{(p_1-p_2)^\mu}{p_1^2-p_2^2}\\ &\quad\times[A_R(p_1)-A_R(p_2)]\Big(\frac{\not{p}_1-\not{p}_2}{2}\Big).\end{aligned}\tag{3.48}$$

Evidently, using that $A_R(\mu)=1$, we have that in the limit $p_1^2=p_2^2=p_3^2=\mu^2$ (and $p_1\sim p_2$) the renormalized vertex $\hat{\Gamma}^\mu_R(p_1,p_2,p_3)$ satisfies

$$\hat{\Gamma}^\mu_R(p_1^2=p_2^2=p_3^2=\mu^2)=\gamma^\mu,\tag{3.49}$$

namely, the standard MOM condition. These considerations provide a concrete renormalization prescription for $\hat{X}(q^2)$. Specifically, the subtractive formula of Eq. (3.40) must be employed, using the closed expressions Eqs. (3.14) and (3.15), substituting $A\longrightarrow A_R$, etc., as dictated by Eq. (3.48).

It turns out that the situation described above applies to all fully dressed PT-BFM vertices considered so far in the ''one-loop dressed'' analysis [15], namely, the three-gluon vertex [appearing in graph (a_1) of Fig. 1] and the ghost-gluon vertex [appearing in graph (a_3)]. As has been explained in detail in various recent works, the requirement of maintaining the WIs of the theory intact leads to the need for introducing gauge-technique Ansätze for the various fully dressed vertices, exactly as happened in the case of the quark-gluon vertex, given in Eq. (3.8). Then, the condition imposed on the renormalization constants forces the renormalized vertices to obey the aforementioned MOM condition.

Let us study how this procedure works in the case of the ghost-gluon vertex, which has a much simpler tensorial structure compared to the three-gluon vertex [64]. At tree level the PT-BFM ghost-gluon vertex has the form $\hat{\Gamma}^{abc}_{\mu 0}(p_1,p_2,p_3)=f^{abc}(p_2-p_1)_\mu$; note that, in contradistinction to the asymmetric ghost-gluon vertex known from the R_ξ gauges, the momenta of both the ghost and the antighost enter now. The all-order WI satisfied by this vertex is given by [15]

$$p_3^\mu\hat{\Gamma}_\mu(p_1,p_2,p_3)=D^{-1}(p_1)-D^{-1}(p_2).\tag{3.50}$$

We renormalize by setting $D_R(p)=Z_c^{-1}D(p)$ and $\hat{\Gamma}^\mu_R(p_1,p_2,p_3)=Z_{1c}\Gamma^\mu(p_1,p_2,p_3)$; then, Eq. (3.50) implies that $Z_c=Z_{1c}$. In the MOM scheme we require that $D_R^{-1}(p^2=\mu^2)=\mu^2$, which, at the level of the ghost dressing function, translates to the condition $F^{-1}(p^2=\mu^2)=1$ [see also discussion below Eq. (3.31)]. At this point, let us introduce for $\hat{\Gamma}^\mu$ the gauge-technique Ansatz

$$\hat{\Gamma}^\mu(p_1,p_2,p_3)=(p_2-p_1)^\mu\Big[\frac{D^{-1}(p_1)-D^{-1}(p_2)}{p_1^2-p_2^2}\Big],\tag{3.51}$$

such that the WI of Eq. (3.50) is automatically satisfied. Then, multiplying it by Z_c, and following the previous procedure, we obtain for $\hat{\Gamma}^\mu_R(p_1,p_2,p_3)$ (written in terms of the dressing function F)

$$\hat{\Gamma}^\mu_R(p_1,p_2,p_3)=(p_2-p_1)^\mu\times\Big[\frac{p_1^2F_R^{-1}(p_1)-p_2^2F_R^{-1}(p_2)}{p_1^2-p_2^2}\Big].\tag{3.52}$$

In the limit $p_1^2=p_2^2=\mu^2$ the quantity in the square bracket goes to unity, and one recovers the tree-level expression for $\hat{\Gamma}^\mu$.

A similar, but much more cumbersome analysis may be followed for the three-gluon vertex, leading to exactly the same conclusion. In doing so, one must make use of the various closed expressions appearing in [64], where the corresponding gauge-technique Ansatz was first constructed. Finally, the four-gluon and two-gluon–two-ghost vertices appearing in the two-loop diagrams of Fig. 1 are expected to follow exactly the same pattern, given that they too satisfy QED-like WIs [15].

We end this subsection by pointing out an interesting fact. The discussion presented above may lead to the impression that within the PT-BFM framework the corresponding β function is uniquely determined, given that the basic vertices must renormalize according to the standard MOM, due to the QED-like WIs they satisfy. Note, however, that the conventional three-gluon vertex (i.e. the one connecting three quantum gluons, instead of a background and two quantum gluons) appears inside diagram (a_6) in Fig. 1. Eventually, this vertex must also be renormalized [this adds at least one more loop to the two-loop (a_6)], and its renormalization condition is no longer restricted to be identical with that of the propagator, given that it satisfies a complicated STI [65] instead of a WI.

E. The transition to Euclidean space

The actual calculations will be carried out in the Euclidean space, and the various relevant formulas, most notably (2.20) and (3.41), must be modified accordingly. In particular, the integral measure is given by

$$\begin{aligned}\int_k &= i\int_{k_E}=\frac{i}{(2\pi)^d}\frac{\pi^{(d-1)/2}}{\Gamma(\frac{d-1}{2})}\\ &\quad\times\int_0^\pi d\theta\sin^{d-2}\theta\int_0^\infty dy y^{(d/2)-1},\end{aligned}\tag{3.53}$$

where $y=k^2$. When $d=4$, this reduces to

$$\int_k=\frac{i}{(2\pi)^3}\int_0^\pi d\theta\sin^2\theta\int_0^\infty dy y=\frac{i}{(2\pi)^3}\int_E,\tag{3.54}$$

which is the measure employed in our final results. In addition, we will use the standard formulas that allow the transition of the various Green's functions from the physical Minkowski momentum q^2 to the Euclidean $q_{\rm E}^2 = -q^2 > 0$; specifically

$$\begin{aligned} \Delta_{\rm E}(q_{\rm E}^2) &= -\Delta(-q_{\rm E}^2); \\ F_{\rm E}(q_{\rm E}^2) &= F(-q_{\rm E}^2); \\ G_{\rm E}(q_{\rm E}^2) &= G(-q_{\rm E}^2), \end{aligned} \tag{3.55}$$

and

$$A_{\rm E}(q_{\rm E}^2) = A(-q_{\rm E}^2), \qquad B_{\rm E}(q_{\rm E}^2) = B(-q_{\rm E}^2). \tag{3.56}$$

The Euclidean version of $\hat{X}(q^2)$ is defined as the result of the aforementioned operations at the level of (3.14), but with the imaginary factor i that comes from the measure absorbed by the factor of i multiplying $\hat{X}(q^2)$ in Eq. (2.20) or (3.41). Effectively, this amounts to the substitution $i\hat{X}(q^2) \to -\hat{X}_{\rm E}(q_{\rm E}^2)$ where the $\hat{X}_{\rm E}(q_{\rm E}^2)$ is obtained from (3.14) by replacing $\int_k \to \int_{k_{\rm E}}$ (no more i) euclideanizing the momenta ($q^2 \to -q_{\rm E}^2$, $k^2 \to -k_{\rm E}^2$), and using (3.56). Then, the Euclidean version of (2.20) becomes (we suppress the subscript "E" throughout)

$$\Delta_Q(q^2) = \frac{\Delta(q^2)}{1 + \{\hat{X}(q^2)[1 + G(q^2)]^{-2} + \lambda^2\}\Delta(q^2)}. \tag{3.57}$$

The conversion of (3.41) to Euclidean space proceeds following exactly analogous steps.

One may carry out two elementary checks of the expression given in (3.57). First, in the IR limit, $q^2 = 0$, after using (3.16), $\Delta^{-1}(0) = m^2(0)$, and the definition of λ^2 in (2.18), we obtain $\Delta_Q^{-1}(0) = m_Q^2(0)$, as we should.

In the opposite limit, where q^2 acquires large values compared to all mass scales involved, we substitute into Eq. (3.57) the perturbative one-loop results, keeping terms up to order α_s. The Euclidean version of (A11) is determined following the steps described above; specifically, since

$$i\hat{X}^{[1]}(q^2) = -\frac{\alpha_s}{6\pi} q^2 \ln(-q^2/\mu^2), \tag{3.58}$$

then (restoring the E for this step only)

$$\begin{aligned} \hat{X}_{\rm E}^{[1]}(q_{\rm E}^2) &= \left\{\frac{\alpha_s}{6\pi} q^2 \ln(-q^2/\mu^2)\right\}_{q^2 \to -q_{\rm E}^2} \\ &= -\frac{\alpha_s}{6\pi} q_{\rm E}^2 \ln(q_{\rm E}^2/\mu^2). \end{aligned} \tag{3.59}$$

Combining this with the standard result

$$[\Delta^{-1}(q^2)]^{[1]} = q^2\left[1 + \frac{13 C_A \alpha_s}{24\pi} \ln(q^2/\mu^2)\right], \tag{3.60}$$

we obtain from (3.57) (with n_f quark flavors, and $C_A = 3$)

$$[\Delta_Q^{-1}(q^2)]^{[1]} = q^2\left[1 + \frac{\alpha_s}{8\pi}\left\{13 - \frac{4}{3} n_f\right\} \ln(q^2/\mu^2)\right], \tag{3.61}$$

which is the correct one-loop result (in the Landau gauge).

In the derivation given above, the perturbative expression for G, namely ($C_A = 3$),

$$1 + G^{[1]}(q^2) = 1 + \frac{9\alpha_s}{16\pi} \ln(q^2/\mu^2), \tag{3.62}$$

was not necessary, since its inclusion in Eq. (3.57) gives contributions of $\mathcal{O}(g^4)$; however, (3.62) is needed for a final check. Specifically, as is well known, due to the QED-like WIs characteristic of the PT-BFM scheme, the PT-BFM propagator, usually denoted by $\hat{\Delta}$, captures the running of the gauge coupling (β function), for any value of the gauge-fixing parameter. $\hat{\Delta}$ and Δ are related by the all-order relation [42,66]

$$\hat{\Delta}^{-1}(q^2) = [1 + G(q^2)]^2 \Delta^{-1}(q^2), \tag{3.63}$$

whose perturbative expansion yields

$$[\hat{\Delta}_Q^{-1}(q^2)]^{[1]} = q^2\left[1 + \frac{\alpha_s}{48\pi}\{33 - 2n_f\} \ln(q^2/\mu^2)\right], \tag{3.64}$$

namely, the correct one-loop result.

IV. NUMERICAL RESULTS

In this section we will first review the lattice data for the quenched gluon propagator $\Delta(q^2)$ and ghost dressing function $F(q^2)$, and the nonperturbative expressions of the quark functions $A(p^2)$ and $B(p^2)$, obtained in [31] from the solution of the quark-gap equation. With all necessary ingredients available, i.e., $\Delta(q^2)$, $F(q^2)$, $A(q^2)$, and $B(q^2)$, we then evaluate numerically the integrals that determine the contribution of the quark loop, $\hat{X}(q^2)$ (BC vertex), and $\hat{X}^{\rm CP}(q^2)$ (CP vertex), given by Eqs. (3.14) and (3.20), respectively. Finally, with the quark-loop contribution at our disposal, we proceed to estimate through Eq. (3.57) the effect of unquenching, namely, how the overall shape of the quenched propagator $\Delta(q^2)$ is affected by the presence of the quark loops. Finally, we compare the resulting dressing function with that obtained from unquenched lattice simulations. Given the amount of information presented in this section, we have organized the material in four subsections and have enumerated the main points of each subsection to facilitate the perusal.

A. Ingredients

(i) The starting point of our numerical analysis are the quenched $SU(3)$ lattice results for the gluon propagator $\Delta(q^2)$ and ghost dressing function $F(q^2)$ [7]. These are shown, respectively, in the left and right panels of Fig. 7, for three different renormalization points ($\mu = 4.3$, 3.0, and 2.5 GeV). In the same figure we also plot the corresponding fits for the three different renormalization points.

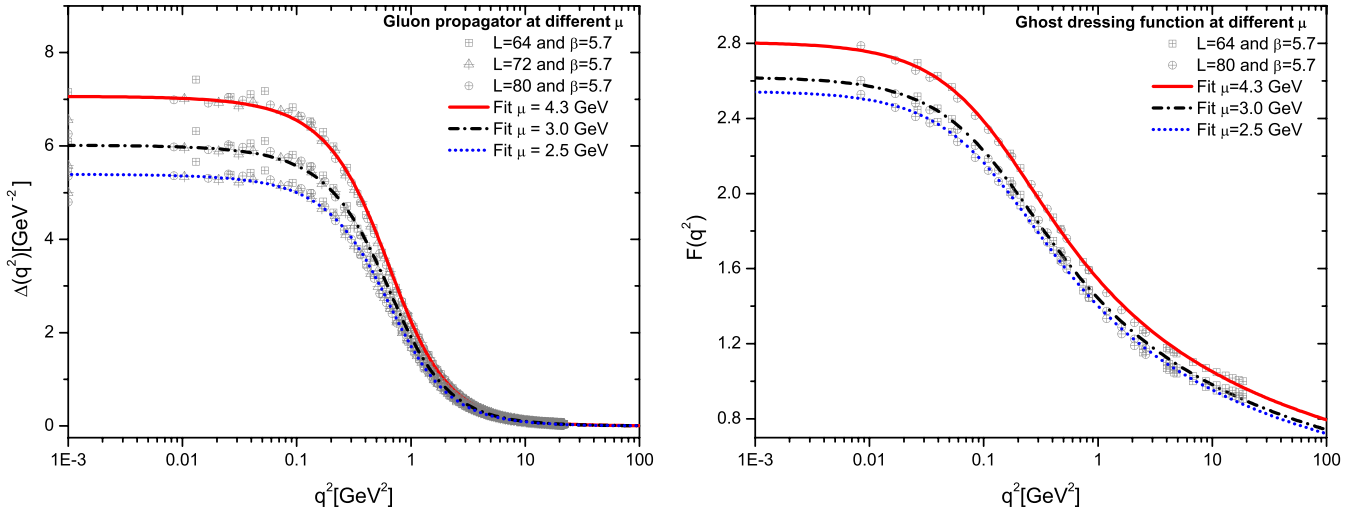

FIG. 7 (color online). Lattice result for the $SU(3)$ gluon propagator (left panel) and ghost dressing function (right panel) renormalized at three different points: $\mu = 4.3$ GeV (solid red curve), $\mu = 3.0$ GeV (dash-dotted black curve), and $\mu = 2.5$ GeV (dotted blue curve).

The explicit functional form used for the gluon propagator fit is given by

$$\Delta^{-1}(q^2) = m_g^2(q^2) + q^2\left[1 + \frac{13 C_A g_1^2}{96\pi^2}\ln\left(\frac{q^2 + \rho_1 m_g^2(q^2)}{\mu^2}\right)\right], \quad (4.1)$$

where

$$m_g^2(q^2) = \frac{m_0^4}{q^2 + \rho_2 m_0^2}, \quad (4.2)$$

with $m_0 = 520$ MeV, $g_1^2 = 5.68$, $\rho_1 = 8.55$, and $\rho_2 = 1.91$ for $\mu = 4.3$ GeV.

For the ghost dressing function we use

$$F^{-1}(q^2) = 1 + \frac{9}{4}\frac{C_A g_2^2}{48\pi^2}\ln\left(\frac{q^2 + \rho_3 m_g^2(q^2)}{\mu^2}\right); \quad m_g^2(q^2) = \frac{m_0^4}{q^2 + \rho_4 m_0^2}, \quad (4.3)$$

with the parameters given by $m_0 = 520$ MeV, $g_2^2 = 8.65$, $\rho_3 = 0.25$, and $\rho_4 = 0.64$.

We emphasize that the quantities g_1^2 and g_2^2 appearing in the above expressions for the fits are not to be identified with the real coupling constant of the theory (denoted by g^2). Both expressions given in Eqs. (4.1) and (4.3) are simply physically motivated fits, simulating, to some extent, the one-loop behavior of the gluon propagator and the ghost dressing function in the presence of themasses. Therefore, the values quoted for the adjustable parameters g_1^2 and g_2^2 must be distinguished from the one used for the real coupling constant g^2 appearing in the definition of $\hat{X}(q^2)$ given in Eq. (3.14). The actual values we have used for the physical g^2 are discussed in Sec. IV C, item (viii).

Because of the multiplicative renormalizability, the fit for the gluon propagator renormalized at $\mu = 3.0$ GeV (dash-dotted black curve) and $\mu = 2.5$ GeV (dotted blue curve) can be obtained by a simple rescaling of Eq. (4.1). More specifically, we should divide them by the factors of 1.17 and 1.31, respectively. In the case of the ghost dressing function, we should rescale Eq. (4.3) by 1.07 and 1.10.

(ii) Next, the computation of the quark contribution $\hat{X}(q^2)$ and $\hat{X}^{CP}(q^2)$ [Eqs. (3.14) and (3.20)] requires the knowledge of the nonperturbative behavior of the functions $A(k^2)$ and $B(k^2)$ appearing in the definition of the full quark propagator (3.7). Both functions can be determined by solving numerically the quark-gap equation; however, one has to be particularly careful about how the non-Abelian quark-gluon vertex, which enters in the latter equation, is approximated. Note, in particular, that, as discussed in detail in [31], the quark-gap equation is identical within both the conventional and the PT-BFM frameworks. As a result, the quark-gluon vertex entering in it is Γ_μ (and not $\hat{\Gamma}_\mu$), satisfying the STI given in Eq. (3.3). This fact, in turn, introduces a numerically crucial dependence on the ghost dressing function and the quark-ghost scattering amplitude. Once these effects are duly taken into account, and the BC or CP vertices improved accordingly [31], one can solve the resulting nonlinear system of integral equations for $A(k^2)$ and $B(k^2)$, supplemented by the lattice gluon propagator and ghost dressing function mentioned above.

(iii) The results obtained following the outlined procedure are shown in Fig. 8 (for the specific value $\mu = 4.3$ GeV in this case). In particular, in the left panel we plot the inverse of the quark wave function $A^{-1}(k^2)$ for the improved BC vertex (dotted black curve), and the "improved" CP vertex (dashed blue curve); in the right panel we show the corresponding solutions for the $B(k^2)$ function. At this point the momentum dependence of the

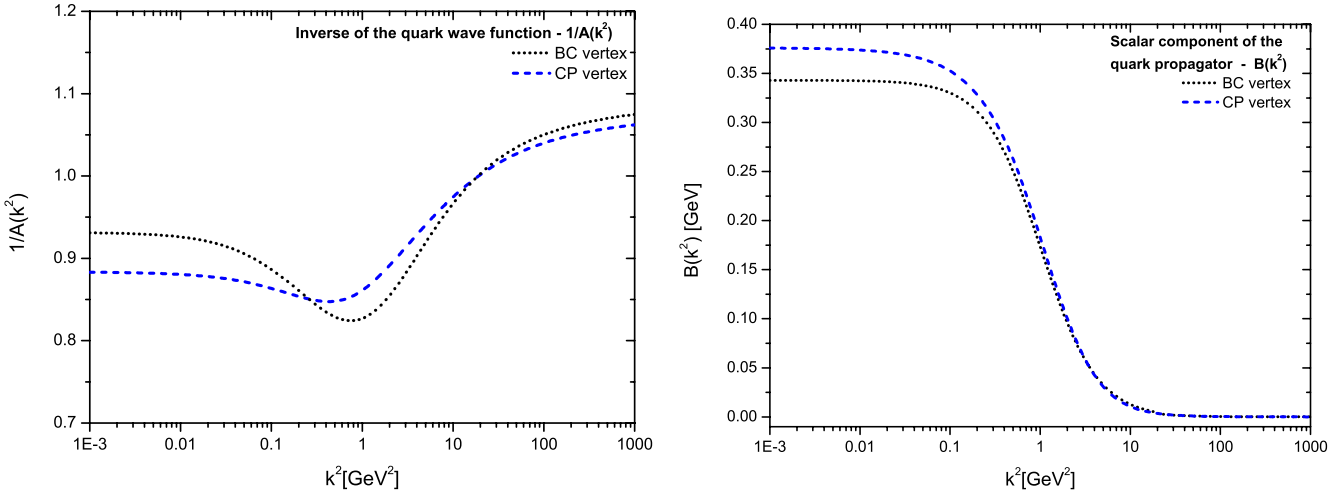

FIG. 8 (color online). Solution of the quark-gap equation: $A^{-1}(k^2)$ (left panel) and $B(k^2)$ (right panel) renormalized at $\mu = 4.3$ GeV. Dotted black curves correspond to the improved BC vertex, while dashed blue curves correspond to the improved CP vertex.

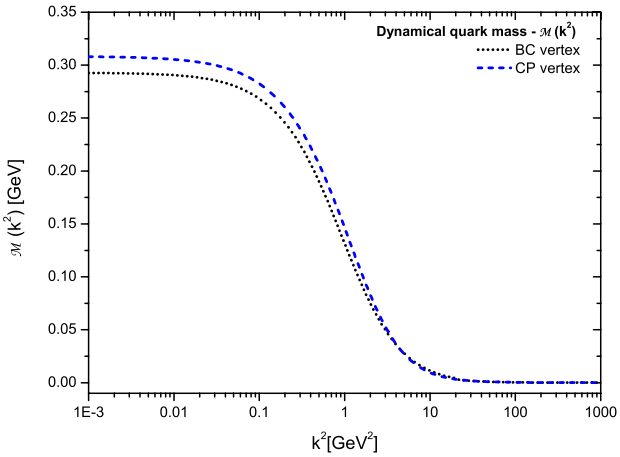

FIG. 9 (color online). The momentum dependence of the dynamical quark mass $\mathcal{M}(k^2) = B(k^2)/A(k^2)$, using the same conventions as in the previous plot.

dynamical quark mass $\mathcal{M}(k^2)$ can be straightforwardly obtained, since $\mathcal{M}(k^2) = B(k^2)/A(k^2)$, and is plotted in Fig. 9, for the two forms of the quark-gluon vertex considered. Clearly the two results coincide in the UV, whereas in the IR we notice that the CP vertex produces the slightly higher value $\mathcal{M}(0) = M = 307$ MeV when compared with the BC vertex result $M = 292$ MeV. Note, finally, that the results presented have been obtained in the chiral limit, where no "current" mass has been used when solving the gap equation.

B. The quark loop

We can now proceed to the numerical evaluation of the full quark loop, namely, $\hat{X}(q^2)$ (BC vertex) and $\hat{X}^{\rm CP}(q^2)$ (CP vertex), as given by Eqs. (3.14) and (3.20), respectively.

(i) In the left panel of Fig. 10 we show the results obtained for each individual contribution of $\hat{X}(q^2)$, as expressed in Eqs. (3.14) and (3.15). As can easily be seen, the leading contribution comes from the T_1 term, which, as shown in the Appendix, is also the term responsible for the appearance of the perturbative logarithm; the T_2 and T_3 contributions are instead subdominant.

(ii) In the right panel of Fig. 10, we show the same quantities for the $\hat{X}^{\rm CP}(q^2)$ term. In this case, one has the additional contribution $\delta\hat{X}(q^2)$, given in Eq. (3.21), coming from the inclusion of the transverse part of the quark-gluon vertex. The net numerical effect is that the latter term will almost completely cancel the subdominant terms T_2 and T_3, so that the T_1 term practically coincides with the full answer.

(iii) The results for the quark loops $\hat{X}(q^2)$ and $\hat{X}^{\rm CP}(q^2)$ are finally compared in Fig. 11 for the $n_f = 2$ case. It is important to notice that, indeed, $\hat{X}(0) = \hat{X}^{\rm CP}(0) = 0$, as we had previously announced.

C. Effect on the gluon propagator

(i) The next step is to compute the unquenched gluon propagator given in Eq. (3.57). The first thing we should notice is the presence of the auxiliary function $1 + G(q^2)$ in the denominator of Eq. (3.57). Using the fact that, in the Landau gauge, $L(q^2)$ is numerically suppressed [50,51], it follows immediately from Eq. (2.7) that $1 + G(q^2) \approx F^{-1}(q^2)$.

(ii) Substituting into Eq. (3.57) the results for $\Delta(q^2)$ and $F(q^2)$, renormalized at $\mu = 4.3$ GeV and presented in Fig. 7, together with either $\hat{X}(q^2)$ (BC vertex) or $\hat{X}^{\rm CP}(q^2)$ (CP vertex) of Fig. 11, we obtain the results shown in the left panel of Fig. 12. As before, the dotted black curve represents the result for the case where we employ the BC vertex, while the dashed blue curve is for the CP vertex. We clearly see that the unquenched gluon propagator suffers a

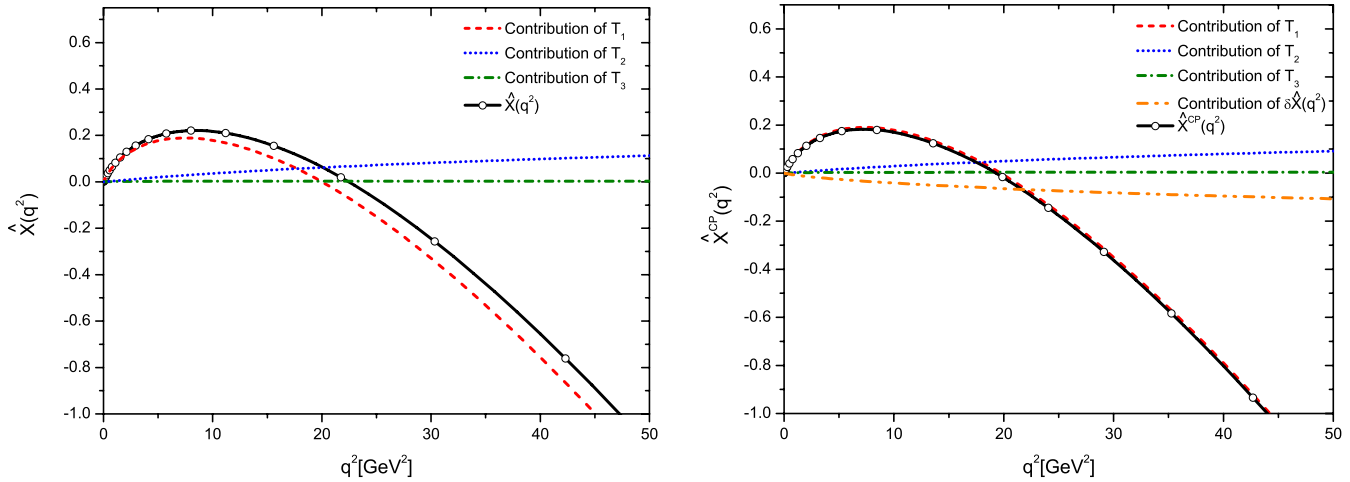

FIG. 10 (color online). Individual contributions of the terms proportional to T_1 (dashed red curve), T_2 (dotted blue line), T_3 (dash-dotted green), and $\delta\hat{X}(q^2)$ (dashed with two dots orange curve), to $\hat{X}(q^2)$ (left panel) and $\hat{X}^{\rm CP}(q^2)$ (right panel), respectively. The sum of all contributions produce in both cases the continuous (black with white circles) curve, which represent the full quark-loop contribution to the gluon propagator.

sizable suppression in the intermediate momenta region compared to the quenched case (solid red curve). Notice that, in this particular case (left panel of Fig. 12) we have set $\lambda^2 = 0$, and therefore, the three curves coincide at $q^2 = 0$, since $\hat{X}(0) = \hat{X}^{\rm CP}(0) = 0$.

(iii) As mentioned before, because of our present limitation in determining the precise value of λ^2, we will restrict ourselves to extracting an approximate range for λ^2, through the extrapolation of the curves in the region delimited by the shaded area shown in the left panel of Fig. 12.

Specifically, we perform a one-dimensional extrapolation in the deep IR region using as input the result obtained for the quenched gluon propagator in the middle IR and intermediate regions. The first step is to select the momentum from which $\Delta_Q(q)$ is extrapolated. We choose three different points, namely, (i) 0.02 GeV^2, (ii) 0.05 GeV^2, and (iii) 0.07 GeV^2, and implement the extrapolation starting for each of these points. In all three cases, we extrapolate the data up to $q^2 = 10^{-3}$ GeV^2 using the cubic B-spline method. We basically split each of these ranges into 150 pieces and fit each segment with a cubic Bezier spline. The goal is to get a fit segment that is smooth in the first derivative and continuous in the second derivative, both within an interval and at its boundaries. When these boundary conditions are met, the entire function is constructed in a piecewise manner.

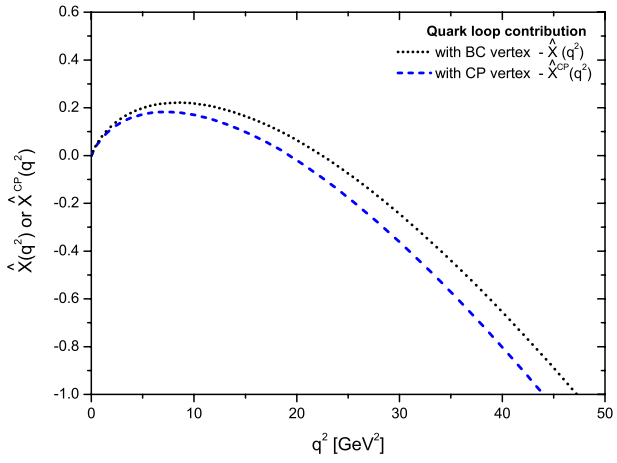

FIG. 11 (color online). Comparison between the contributions of the quark loop $\hat{X}(q^2)$ (dotted black curve) and $\hat{X}^{\rm CP}(q^2)$ (dashed blue curve) to the gluon self-energy with $n_f = 2$.

In the right panel of Fig. 12, we show $\Delta_Q(q^2)$ when the extrapolation is done for values of momenta smaller than $q^2 = 0.05$ GeV^2. As we can clearly see, the tendency of the unquenched gluon propagator is always to be below the quenched one (solid red curve), no matter whether we use the BC vertex (dotted black curve) or the CP vertex (dashed blue curve).

Now, we are in position to determine the order of magnitude of $m_Q^2(0)$ and λ^2. Combining Eqs. (2.15) and (2.18) and the data presented in the right panel of Fig. 12, we found the values of $m_Q^2(0) = 0.156$ GeV^2, $m^2(0) = 0.142$ GeV^2, and $\lambda^2 = 0.014$ GeV^2 for the BC vertex, whereas for the CP we have $m_Q^2(0) = 0.151$ GeV^2 and $\lambda^2 = 0.009$ GeV^2. These results suggest that the effective gluon mass increases when we include the quark loops in the gluon self-energy.

In addition, notice that the results obtained with the BC and CP vertices differ only by approximately 3%. Since this difference is rather small and does not cause significant changes in what follows, for the rest of our analysis we will focus on the BC vertex only.

(iv) It is important to verify whether the IR suppression, shown in the unquenched propagator of the right panel of Fig. 12, persists when we start the curve extrapolation from different values. This is shown in Fig. 13, where we compare the results obtained when we extrapolate $\Delta_Q(q^2)$ (with the

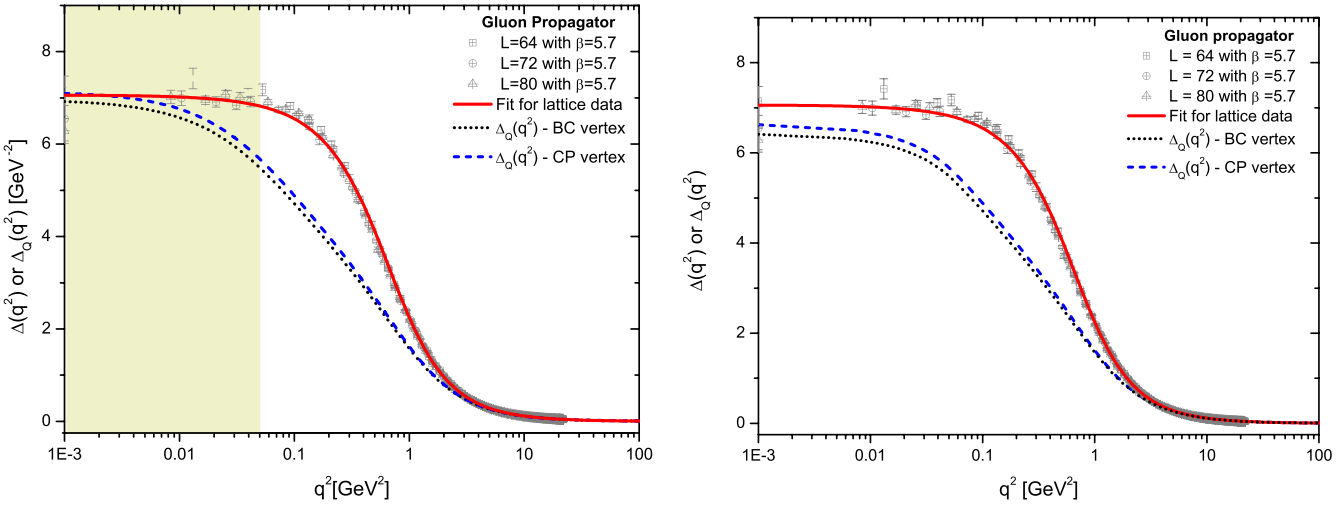

FIG. 12 (color online). The unquenched gluon propagator $\Delta_Q(q^2)$ when no extrapolation is used, i.e. $\lambda^2 = 0$ in Eq. (3.57) (left panel). The dotted black curve represents the unquenched propagator obtained with the BC vertex, whereas the dashed blue curve represents the result for the CP vertex. The result for $\Delta_Q(q^2)$ when the extrapolation is performed in the shade area, i.e. from $q^2 = 0.05$ GeV^2 toward the deep IR (right panel).

BC vertex) from momenta below $q^2 = 0.02$ GeV^2 (dash-dotted green line), $q^2 = 0.05$ GeV^2 (dashed with two dots magenta line), and $q^2 = 0.07$ GeV^2 (dashed orange line).

Indeed, we can see that the general trend, for all cases, is that the unquenched propagator $\Delta_Q(q^2)$ displays suppressed intermediate and IR regions, when compared to the quenched case. In particular, for the extrapolation starting at $q^2 = 0.02$ GeV^2 we can see that $m_Q^2(0) = 0.147$ GeV^2 and $\lambda^2 = 0.005$ GeV^2, whereas when we extrapolate from $q^2 = 0.07$ GeV^2 we obtain $m_Q^2(0) = 0.163$ GeV^2 and $\lambda^2 = 0.021$ GeV^2. Therefore, the extrapolations mentioned above produce a range of possible values for $\Delta_Q(0)$ or, equivalently, $m_Q^2(0)$ indicated by the yellow striped band in Fig. 13, where the difference between the upper value and the lower value is approximately 10%. Thus, the general conclusions we can draw with respect to the properties of the unquenched propagator are quite insensitive to the extrapolation point used (and therefore, ultimately, to the value of λ). In what follows we will further explore the properties of $\Delta_Q(q^2)$ extrapolated toward the IR starting from $q^2 = 0.05$ GeV^2.

In the left panel of Fig. 14 we superimpose the quenched lattice result of [7] (solid red curve) and the unquenched result obtained from our calculation (dotted black curve), while in the right panel we show a comparison of the corresponding dressing functions. In the latter case notice that, as expected, both the quenched and unquenched curves vanish at zero momentum transfer, and their differences in the deep IR region are completely washed out. A direct comparison between the unquenched dressing function computed here and that obtained in the unquenched lattice simulation of [6] is postponed for the next subsection.

(v) The dependence of the unquenched solution on the number of the flavors n_f is next shown in Fig. 15. As in previous plots, we show the quenched lattice data (solid red curve) as a benchmark, while different dashed and/or dotted curves correspond to different values of flavors: $n_f = 1$ (dash-dotted green curve), $n_f = 2$ (dotted black curve), and, finally, $n_f = 3$ (dashed blue curve). Evidently, increasing the number of flavors results in a more suppressed gluon propagator. As can be seen clearly in Fig. 15, in the IR and intermediate regions the curves with more active quarks lie below the ones with fewer. This fact does

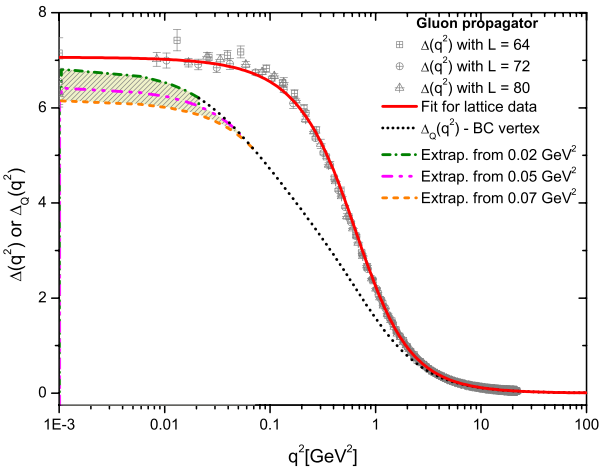

FIG. 13 (color online). Comparison between the quenched $\Delta(q^2)$ and the unquenched $\Delta_Q(q^2)$ gluon propagators. The yellow striped band shows the possible values that $\Delta_Q(0)$ can assume at zero momentum. The two curves delimiting the band represent the extrapolation toward the IR either starting from 0.02 GeV^2 (dash-dotted green line) or 0.07 GeV^2 (dashed orange line). The dashed with two dots magenta curve corresponds to an extrapolation of the numerical result starting from the intermediate value 0.05 GeV^2.

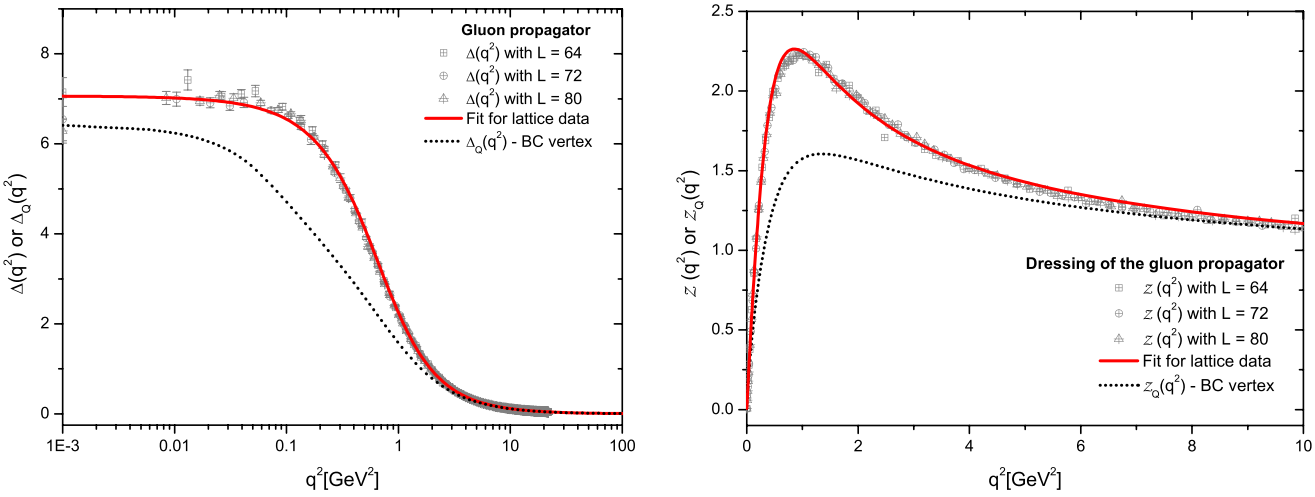

FIG. 14 (color online). The quenched (solid red curve) and unquenched (dotted black curve) gluon propagators (left panel) and dressing functions (right panel). The unquenched case corresponds to the case where the extrapolation starts at $q^2 = 0.05$ GeV^2.

not contradict the one-loop perturbative behavior, given by Eq. (3.61), stating that, in the UV, $\Delta_Q(q^2)$ increases for a higher number of quark families. Indeed, we have checked that the perturbative behavior of $\Delta_Q(q^2)$ is recovered, due to a crossing that takes place around the renormalization point μ, which makes the curve for $n_f = 3$ (dashed blue curve) go above all the others in the perturbative regime.

(vi) In Fig. 16 we show another interesting property of $\Delta_Q(q^2)$. The dotted black curve represents $\Delta_Q(q^2)$ obtained with the nonperturbative expression for $\hat{X}(q^2)$ given by Eqs. (3.14) and (3.15); the dash-dotted blue curve refers instead to the result of a simple one-loop calculation with a constant quark mass [see Eq. (A5) in the Appendix]. Notice that the latter result can be obtained by substituting $A_a = A_b = 1$ and $B_a = B_b = 292$ MeV into Eqs. (3.14) and (3.15). The difference between the two curves is at the few percent level, in agreement with the observation made before that the terms T_2 and T_3 are numerically subdominant (at the one-loop level these terms vanish, since $L_2 = L_3 = 0$). These observations suggest that the nonperturbative quark-loop diagram (a_{11}) appears to be rather insensitive to the running of the dynamical quark mass.

(vii) To check the decoupling of the heavier flavors, we also compare in the right panel of the same figure the result of the one-loop calculation with $M = 292$ MeV (dash-dotted blue curve) and $M = 1$ GeV (dashed green curve). As we see clearly, the effect of the dynamical fermions on the gluon propagator becomes progressively suppressed as the quark mass increases.

(viii) Up to now, we have computed the unquenched gluon propagator $\Delta_Q(q^2)$ for a particular fixed value of the renormalization point μ, namely, $\mu = 4.3$ GeV. It is well known that both quenched and unquenched gluon propagators are μ-dependent quantities, and therefore, different choices of μ will lead to different results.

In order to address quantitatively this effect, in the left panel of Fig. 17 we show $\Delta_Q(q^2)$ with $n_f = 2$ for three different values of μ: (i) $\mu = 2.5$ GeV and $\alpha_s = 0.461$ (dotted blue curve); (ii) $\mu = 3.0$ GeV and $\alpha_s = 0.395$ (dash-dotted black curve), and (iii) $\mu = 4.3$ GeV and $\alpha_s = 0.295$ (solid red curve). Details on how the values of α_s corresponding to each renormalization point were determined can be found in [32,51]. From Fig. 17 one can then clearly see that higher values of μ correspond to larger values of $\Delta_Q(0)$, which is basically the same pattern observed for the quenched case.

(ix) Finally, one important property that relates the gluon propagators renormalized at different values of μ is the multiplicative renormalizability, which allows one to connect a set of data renormalized at μ with a corresponding set renormalized at ν, through the relation

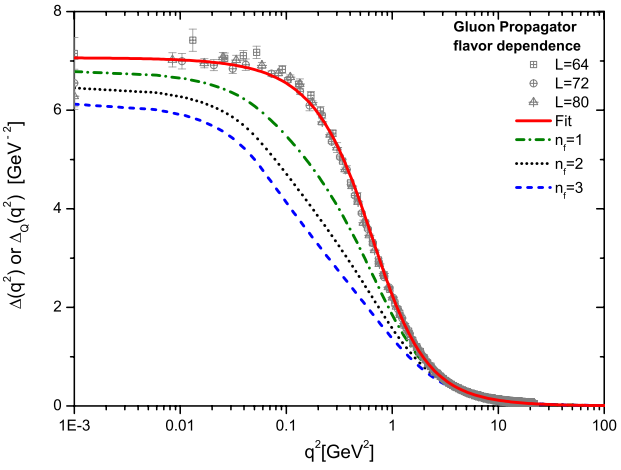

FIG. 15 (color online). The unquenched gluon propagator for different number of flavors: $n_f = 1$ (dash-dotted green curve), $n_f = 2$ (dotted black curve), and $n_f = 3$ (dashed blue curve).

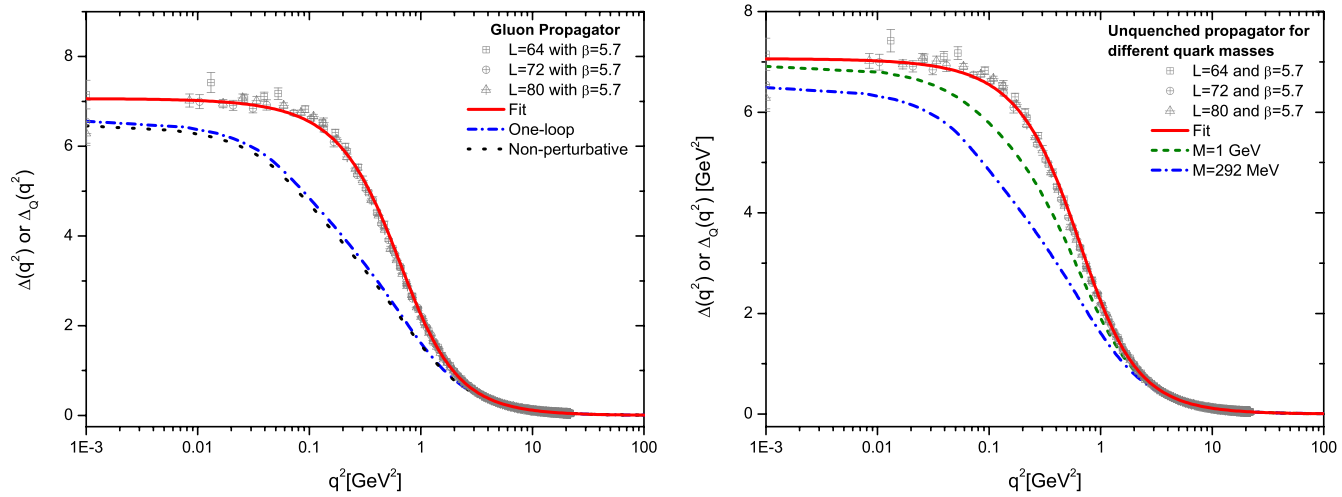

FIG. 16 (color online). Left panel: The unquenched gluon propagator $\Delta_Q(q^2)$ for $n_f = 2$ (dotted black curve) compared to the one-loop dressed result with a constant quark mass $M = 292$ MeV (dash-dotted blue curve). Right panel: The unquenched gluon propagator $\Delta_Q(q^2)$ for $n_f = 2$ with different values of constant quark masses: $M = 1$ GeV (dashed green curve) and $M = 292$ MeV (dash-dotted blue curve).

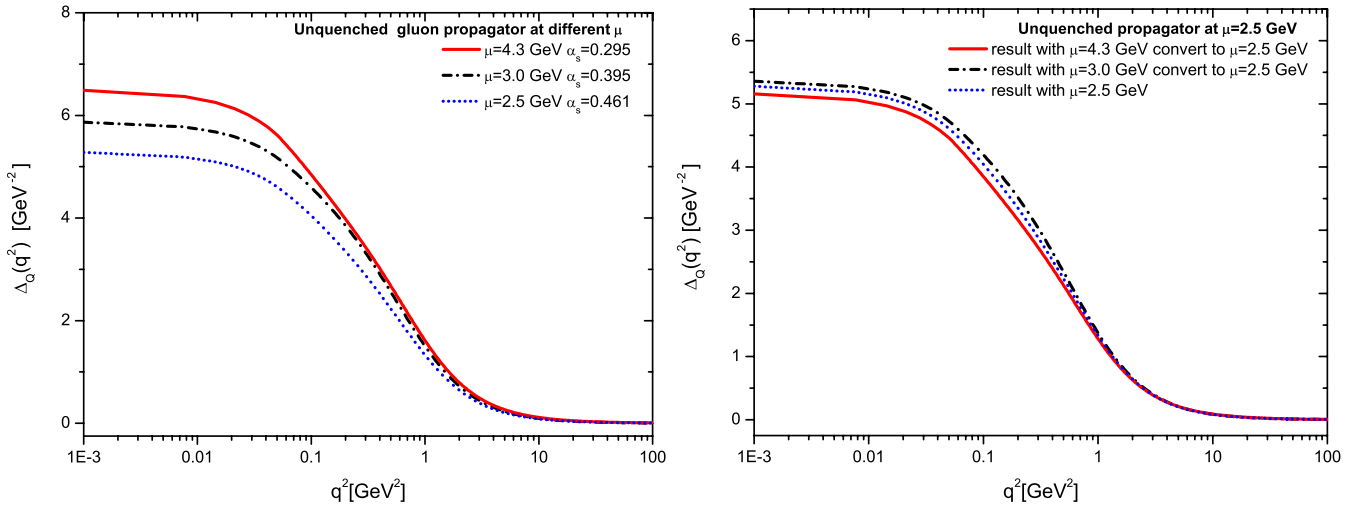

FIG. 17 (color online). Left panel: The $n_f = 2$ unquenched gluon propagator renormalized at different values of μ and α_s: $\mu = 4.3$ GeV and $\alpha_s = 0.295$ (solid red curve), $\mu = 3.0$ GeV and $\alpha_s = 0.395$ (dash-dotted black curve), $\mu = 2.5$ GeV and $\alpha_s = 0.461$ (dotted blue curve). Right panel: All curves shown in the left panel renormalized at the same point $\mu = 2.5$ GeV using Eq. (4.4).

$$\Delta_Q(q^2, \mu^2) = \frac{\Delta_Q(q^2, \nu^2)}{\mu^2 \Delta_Q(\mu^2, \nu^2)}. \tag{4.4}$$

In the right panel of Fig. 17 we check how $\Delta_Q(q^2)$ behaves under changes of μ using Eq. (4.4). Evidently, multiplicative renormalizability would require that the three curves lie on top of each other; however, we see that there is a minor difference between them (at the 4% level), whose origin might be related to the fact that, as discussed in the previous section, in our computation the renormalization procedure was carried out subtractively instead of multiplicatively.

D. Comparison with the lattice data

In this final subsection we carry out a comparison between the results we found for the gluon propagator, Δ_Q, and its dressing function, $\mathcal{Z}_Q(q^2)$, and the data obtained from unquenched lattice simulations [5,6].

We remind the reader that, according to the convention introduced below Eq. (3.7), we will denote by M (with the appropriate flavor index) the value of the corresponding running quark mass $\mathcal{M}(p^2)$ at $p^2 = 0$.

To begin with, in Fig. 18 we compare the $n_f = 2$ lattice data (dark gray stars) of [5] renormalized at $\mu = 4.3$ GeV with our results for two different values of light quark masses $M_{u/d} = 15$ MeV (dashed blue curve) and

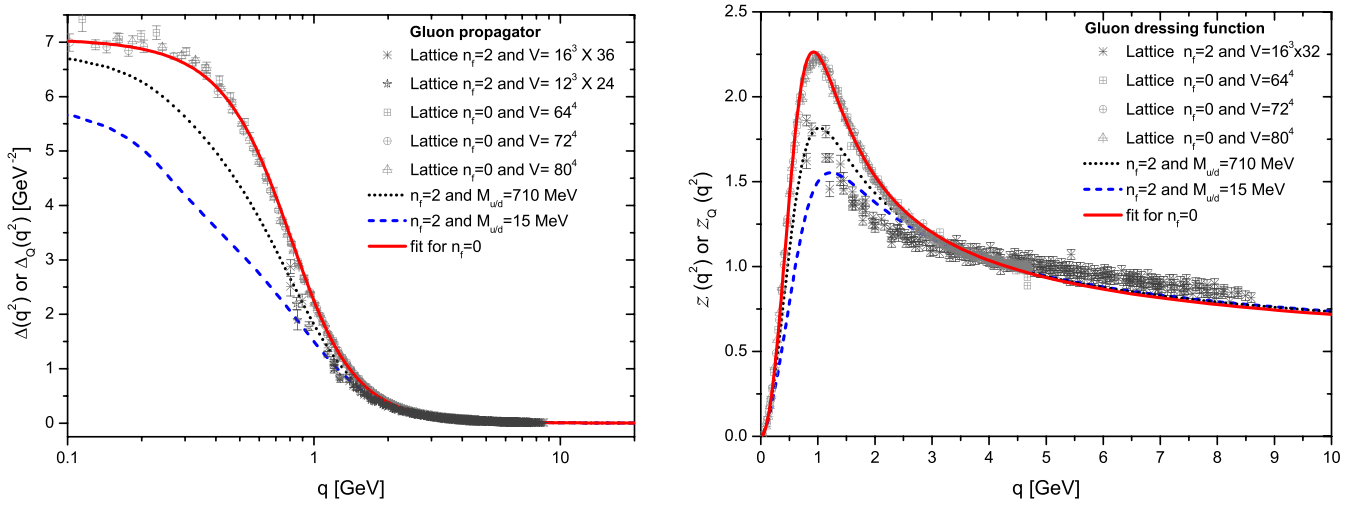

FIG. 18 (color online). The unquenched gluon propagator (left panel) and the gluon dressing function (right panel) obtained in Ref. [5] (dark gray stars), together with the SDE results for two light quarks with $M_{u/d} = 15$ MeV (dashed blue curve) and $M_{u/d} = 710$ MeV (dotted black curve). The quenched lattice results are also displayed for comparison.

$M_{u/d} = 710$ MeV (dotted black curve). This mass range roughly corresponds to the one used in the simulations of [5], which were, however, carried out in relatively small lattices, corresponding to a physical volume of at most $1.5^3 \times 3.1$ fm^4.

Both $\Delta_Q(q^2)$ and its corresponding $\mathcal{Z}_Q(q^2)$ are shown in the left and right panels of Fig. 18, respectively, where one sees a fairly good agreement between our theoretical predictions and the lattice computation. In particular, we see that for the case where $M_{u/d} = 710$ MeV (dotted black curve), one has (in the less favorable region located in the range of momenta between 1 and 2 GeV) a relative error not greater than 20%. To be sure, the bulk of this discrepancy might be stemming from the approximations employed in our SDE analysis; for example, higher quark loops have been omitted from our calculations. On the other hand, the discrepancy in the tail of the plot might be associated with the cylindrical cuts imposed on the lattice data, in order to reduce the hypercubic artifacts [that is, the breaking of the original $O(4)$ symmetry down to $H(4)$ due to the lattice discretization]. This procedure is known to be problematic for large momenta, since as the momentum increases so does the number of excluded configurations, thus introducing additional error to the calculated value of the function of interest (see, e.g., [67] and references therein).

An analogous comparison can be performed for $2 + 1$ flavor QCD, using the data of [6]. In this case the physical volume is much larger (corresponding to $2.4^3 \times 8.3$ fm^4), and therefore the IR behavior of the gluon propagator can be better probed. In Fig. 19, we show the $2 + 1$ flavor QCD lattice data for $\Delta_Q(q^2)$ (left panel) and its corresponding $\mathcal{Z}_Q(q^2)$ (right panel) renormalized at $\mu = 4.3$ GeV, together with our results obtained for two light quarks of mass $M_{u/d} = 292$ MeV and one heavier of $M_h = 500$ MeV (dash-dotted black curve). It is important to mention that the above ranges of quark masses are consistent with the values generally employed in phenomenological calculations [68,69].

We clearly see that the overall shape of the calculated curves display (as was already the case in the $n_f = 2$ comparison) a good agreement with the data in a sizable range of momenta. The region where the difference between the curves is more pronounced is, in the case of the gluon propagator, around $q = 470$ MeV (left panel), where the relative error between lattice and our prediction is around 18% (observe that, for values of momentum larger than 800 MeV, the difference between the curves is at the 10% level or smaller).

In addition, notice that on the same plots we display also the case where $M_{u/d} = 360$ MeV and $M_h = 560$ MeV (dotted blue curve). The way this latter set of mass values (and the corresponding quark propagators) are obtained is by solving the quark-gap equation using suitable values for the current masses. More specifically, for the light quarks (up/down) we use a current mass of 14 MeV, while for the heavier one (strange) we use 68 MeV, in agreement with the values quoted in Ref. [6]. Observe that the dotted blue curve indicates that the increase of masses produces a slight change in the peak of the dressing function.

It would be instructive to analyze how different choices for M_h modify the forms of $\Delta_Q(q^2)$ and $\mathcal{Z}_Q(q^2)$ shown in Fig. 19. Indeed, as we have already shown in Fig. 16, the gluon propagator becomes progressively suppressed as the quark mass increases; it is therefore natural to expect that the gluon dressing function will also be affected by different choices of masses.

In Figs. 20 and 21, we plot the gluon propagator $\Delta_Q(q^2)$ and its corresponding gluon dressing function $\mathcal{Z}_Q(q^2)$ for different values of the heavy quark mass M_h, respectively.

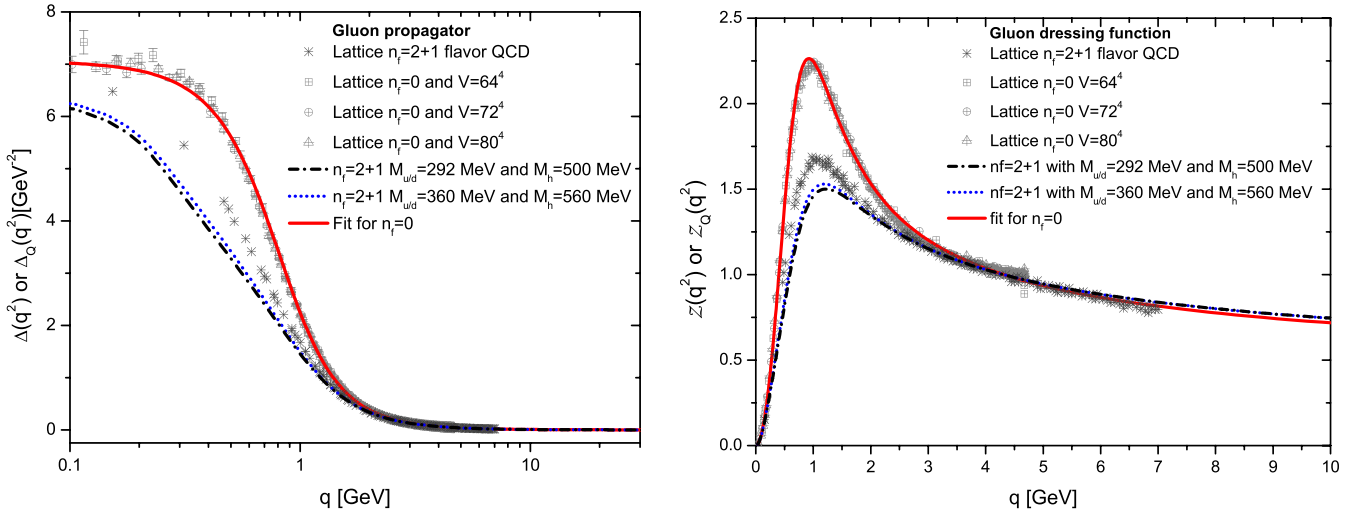

FIG. 19 (color online). The unquenched gluon propagator (left panel) and the gluon dressing function (right panel) obtained in Ref. [6] (dark gray stars), together with the SDE result for two light quarks with $M_{u/d} = 292$ MeV and one heavier with $M_s = 500$ MeV (dash-dotted black curve), and the case where $M_{u/d} = 360$ MeV and $M_s = 560$ MeV (dotted blue curve).

In all curves the light quarks have constant masses of $M_{u/d} = 292$ MeV, whereas for the heavier quark we used $M_h = 292$ GeV (short dashed blue curve), $M_h = 500$ MeV (dashed orange curve), $M_h = 1.0$ GeV (dotted green curve), and $M_h = 1.5$ GeV (dashed with two dots magenta curve).

As it can clearly be seen, the peak of $\mathcal{Z}_Q(q^2)$ becomes more pronounced as we increase the value of M_h. Notice that the case where $M_h = 1.5$ GeV (dashed with two dots magenta curve) is much closer to the lattice data (dark gray stars). In addition, if we keep increasing the heavy quark mass gradually, the observed trend of the results is to move progressively closer to the case where only two quarks are active (dash-dotted black curve), thus confirming the notion of decoupling of heavy flavors. To avoid any possible confusion caused by the striking proximity of the $n_f = 2$ dressing function curve to the lattice data, we reiterate that the real comparison between the (2 + 1) data and the corresponding (2 + 1) SDE result is given in Fig. 19; however, our results seem to suggest that the heavy flavor was effectively decoupled in the simulations of [6].

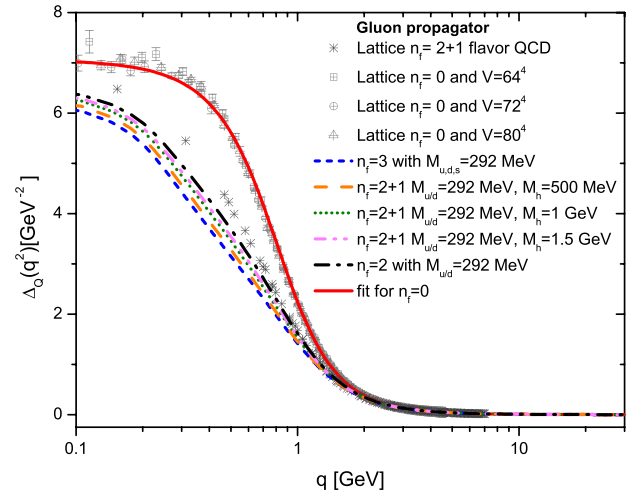

FIG. 20 (color online). The unquenched gluon propagator for $n_f = 2 + 1$ flavors. The light quarks have masses of $M_{u/d} = 292$ MeV, while for the heavier quark: $M_h = 292$ GeV (short dashed blue curve), $M_h = 500$ MeV (dashed orange curve), $M_h = 1.0$ GeV (dotted green curve), and $M_h = 1.5$ GeV (dashed with two dots magenta curve).

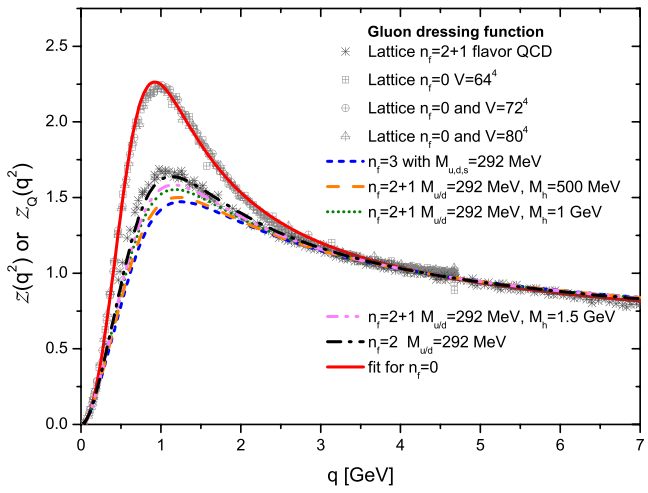

FIG. 21 (color online). The unquenched gluon dressing function for $n_f = 2 + 1$ flavors. The light quarks have masses of $M_{u/d} = 292$ MeV, while for the heavier quark: $M_h = 292$ GeV (short dashed blue curve), $M_h = 500$ MeV (dashed orange curve), $M_h = 1.0$ GeV (dotted green curve), and $M_h = 1.5$ GeV (dashed with two dots magenta curve).

V. CONCLUSIONS

In this article we have presented a general method for estimating the effects that the unquenching induces on the (IR finite) gluon propagator, in the Landau gauge. The basic assumption of the method followed has been that the main bulk of the effect originates from the ''one-loop dressed'' quark diagram, while the rest of the contributions is considered to be subleading. We have restricted the applicability of this approach to a small number of quark families ($n = 1, 2, 3$), where we assume the presence of the quarks does not alter qualitatively the behavior of the quenched propagator. In particular, we expect that the crucial property of IR finiteness will persist; i.e., the gluon mass generating mechanism will not be distorted by the inclusion of a few quark families. In fact, throughout our analysis we use the quenched gluon propagator obtained in $SU(3)$ lattice simulations as our point of reference and estimate the deviations induced to it by the quarks.

The nonperturbative calculation of the quark loop proceeds by means of two suitable Ansätze for the fully dressed quark-gluon vertex $\hat{\Gamma}_\mu$, enforcing the exact transversality of the resulting contribution. The use of the PT-BFM formalism simplifies the form of these Ansätze considerably, due to the ''abelianization'' that it induces, given that the corresponding Green's functions, when contracted with respect to the momentum carried by the background leg, satisfy linear ghost-free WIs instead of the usual nonlinear STIs. This fact, in turn, avoids the explicit reference to the quark-ghost kernel, which appears in the standard STI satisfied by the conventional quark-gluon vertex Γ_μ [the H auxiliary function of Eq. (3.3)]. Of course, one cannot completely eliminate any dependence on H, for the simple reason that it affects the quark-gap equation that determines the quantities $A(p)$ and $B(p)$, namely, the nonperturbative Dirac components of the quark propagator; this happens because, as explained in [31], the quark-gluon vertex entering in the gap equation is Γ_μ and not $\hat{\Gamma}_\mu$. Given that the structure of the quark-ghost kernel is largely unexplored (for an SD estimate of one of its form factors, see [31]), reducing the dependence of the answer on it is clearly advantageous.

The main results of our study is that the inclusion of the quark loop(s) induces a suppression in the intermediate and IR momentum regions, with respect to the quenched case. As emphasized in the main text, the actual saturation point of the unquenched propagator, i.e., the value $\Delta_Q(0)$, normally associated with the IR value of the dynamical gluon mass, $m^2(0)$, is not possible to determine at present, despite the fact that the quark-loop contribution to the corresponding gluon self-energy vanishes at $q^2 = 0$, by virtue of a powerful identity. The reason is that the momentum evolution of the gluon mass depends (in a yet not fully determined way) on the structure of the gluon propagator through the *entire range* of physical momenta; thus, the suppression of the propagator due to the inclusion of the quarks is expected to modify the value of $m^2(0)$. In this work we have adopted a simple hand-waving approach for estimating $\Delta_Q(0)$. Specifically, given that the unquenched propagator in the IR and intermediate regions is consistently below the corresponding quenched curve, we have simply extrapolated toward the point $q^2 = 0$. In practice, the outcome of this simple procedure depends to some extent on the extrapolation details (in particular, what one considers as the last ''faithful'' point), and therefore one can only determine a certain range of ''reasonable'' values for $\Delta_Q(0)$.

The uncertainty associated with the determination of the saturation point is practically eradicated if one considers instead of the gluon propagator its corresponding dressing function. This latter quantity, when compared to the corresponding dressing function of the quenched lattice propagator, clearly demonstrates the aforementioned suppression in the IR and intermediate regions induced by the inclusion of the quarks. The unquenched gluon propagator and its corresponding dressing function obtained through our procedure appears to be in rather good agreement with the lattice results available in the literature.

There are certain theoretical improvements, which, if successfully implemented, would put the proposed approach on a more solid ground. To begin with, it is clear that the full SDE treatment of the problem at hand would entail the *simultaneous* treatment of a complicated set of coupled integral equations, in the spirit presented in [38,39], in the context of the scaling solutions. This type of global treatment appears to be beyond our present calculational powers, mainly due to the plethora of additional technical complications intrinsic to the massive solutions. Instead, we have adopted a step-by-step procedure; for example, the quark-gap equation has been solved ''in isolation,'' and the obtained solutions have been fed into the equations determining the quark loop, and so on. To be sure, this latter procedure might interfere with the nonlinear propagation of certain effects, leading to the corresponding amplification or suppression of various features, and may require additional refinements.

The renormalization properties of the relevant integral equations constitute a commonly known source of theoretical uncertainty, due to the mishandling of the overlapping divergences induced by the well-known intrinsic ambiguity of the gauge technique, related to the unspecified transverse (automatically conserved) part of the vertices. In particular, the BC and CP expressions employed here for the quark-gluon vertex do not fully respect the property of multiplicative renormalizability, which, in turn, leads to dependences on the renormalization point that are not always in accordance with those dictated by the renormalization group. The propagation of such discrepancies to our predictions has been studied numerically and appears to be relatively suppressed. However, more work is clearly needed in order to eliminate the spurious μ dependences. In this vain, it would be interesting, albeit logistically

cumbersome, to explore the effects that other forms of the quark-gluon vertex might have on our predictions, such as those reported in [70,71].

Finally, the reliable calculation of the saturation point $\Delta_Q(0)$ mentioned above hinges explicitly on the derivation of a fully self-consistent integral equation that would determine the momentum evolution of the dynamical gluon mass, both in the quenched case and in the presence of quarks. The derivation of such a complete equation is conceptually and technically rather nontrivial, and is the subject of an ongoing investigation, whose results will hopefully be presented soon.

ACKNOWLEDGMENTS

The research of J. P. is supported by the Spanish MEYC under Grant No. FPA2011-23596. The work of A. C. A is supported by the Brazilian Funding Agency CNPq under Grant No. 305850/2009-1 and Project No. 474826/2010-4.

APPENDIX: THE PERTURBATIVE ONE-LOOP CASE

The textbook perturbative calculation of diagram a_{11} yields (with $d_f = 1/2$)

$$\hat{X}^{[1]}(q^2) = -\frac{2g^2}{d-1}\int_k \frac{dM^2 - (d-2)(k^2 + k\cdot q)}{(k^2 - M^2)[(k+q)^2 - M^2]}, \tag{A1}$$

where M denotes a constant (momentum-independent) mass. Note that the "hat" in this case is redundant, because, at one loop, the conventional and BFM results coincide. The result of Eq. (A1) may be directly recovered from the general case presented in Sec. III, by setting $\mathcal{M}(p) = M$, $A(p) = 1$, $L_1 = 1$, and $L_2 = L_3 = 0$ in Eqs. (3.14) and (3.15).

It is elementary to establish that

$$\hat{X}^{[1]}(0) = 0, \tag{A2}$$

by virtue of the basic identity

$$\int_k \frac{k^2}{(k^2 - M^2)^2} = \frac{d}{2}\int_k \frac{1}{k^2 - M^2}, \tag{A3}$$

or, equivalently,

$$2M^2\int_k \frac{1}{(k^2 - M^2)^2} = (d-2)\int_k \frac{1}{k^2 - M^2}, \tag{A4}$$

whose validity may be easily verified following the integration rules of dimensional regularization. These exact same identities appear in the standard one-loop calculation of the photon vacuum polarization, both in normal QED and in scalar QED, and enforces the masslessness of the photon [54].

The property of (A2) becomes manifest through the use of (A4), which allows one to cast (A1) into the form

$$\hat{X}^{[1]}(q^2) = -\frac{g^2}{d-1}\{(d-2)q^2 I(q^2) + 4M^2[I(q^2) - I(0)]\}, \tag{A5}$$

where

$$I(q^2) = \int_k \frac{1}{(k^2 - M^2)[(k+q)^2 - M^2]}, \tag{A6}$$

or, equivalently, defining

$$u^2(q^2) \equiv q^2 x(x-1) + M^2, \tag{A7}$$

we have

$$\hat{X}^{[1]}(q^2) = -\frac{g^2}{d-1}\left\{(d-2)q^2 I(q^2) - i\frac{M^2}{4\pi^2}\int_0^1 \mathrm{d}x \ln\frac{u^2(q^2)}{M^2}\right\}. \tag{A8}$$

Finally, the renormalized expression for $\hat{X}^{(1)}(q^2)$ in the MOM scheme is given by

$$\hat{X}_R^{[1]}(q^2) = \hat{X}^{[1]}(q^2) - \frac{q^2}{\mu^2}\hat{X}^{[1]}(\mu^2), \tag{A9}$$

giving as a result

$$\hat{X}_R^{[1]}(q^2) = \frac{i\alpha_s}{6\pi}\left\{q^2\int_0^1 \mathrm{d}x \ln\frac{u^2(q^2)}{u^2(\mu^2)} + 2M^2\left[\int_0^1 \mathrm{d}x \ln\frac{u^2(q^2)}{M^2} - \frac{q^2}{\mu^2}\int_0^1 \mathrm{d}x \ln\frac{u^2(\mu^2)}{M^2}\right]\right\}. \tag{A10}$$

Evidently, for q^2 and μ^2 much larger than M^2, one obtains the standard logarithmic correction

$$\hat{X}_R^{[1]}(q^2) = \frac{i\alpha_s}{6\pi}q^2\ln(-q^2/\mu^2). \tag{A11}$$

[1] A. Cucchieri and T. Mendes, Proc. Sci. LAT2007 (2007) 297.
[2] A. Cucchieri and T. Mendes, Phys. Rev. Lett. **100**, 241601 (2008).
[3] A. Cucchieri and T. Mendes, Phys. Rev. D **81**, 016005 (2010).
[4] A. Cucchieri and T. Mendes, Proc. Sci. LATTICE2010 (2010) 280.
[5] W. Kamleh, P. O. Bowman, D. B. Leinweber, A. G. Williams, and J. Zhang, Phys. Rev. D **76**, 094501 (2007).
[6] P. O. Bowman, U. M. Heller, D. B. Leinweber, M. B. Parappilly, A. Sternbeck, L. von Smekal, A. G.

Williams, and J.-b. Zhang, Phys. Rev. D **76**, 094505 (2007).
[7] I. L. Bogolubsky, E. M. Ilgenfritz, M. Muller-Preussker, and A. Sternbeck, Proc. Sci. LATTICE (2007) 290.
[8] I. L. Bogolubsky, E. M. Ilgenfritz, M. Muller-Preussker, and A. Sternbeck, Phys. Lett. B **676**, 69 (2009).
[9] O. Oliveira and P. J. Silva, Phys. Rev. D **79**, 031501 (2009).
[10] O. Oliveira and P. J. Silva, Proc. Sci. LAT2009 (2009) 226.
[11] R. Alkofer and L. von Smekal, Phys. Rep. **353**, 281 (2001).
[12] C. S. Fischer, J. Phys. G **32**, R253 (2006).
[13] A. C. Aguilar and J. Papavassiliou, J. High Energy Phys. 12 (2006) 012.
[14] D. Binosi and J. Papavassiliou, Phys. Rev. D **77**, 061702 (R) (2008).
[15] A. C. Aguilar, D. Binosi, and J. Papavassiliou, Phys. Rev. D **78**, 025010 (2008).
[16] D. Binosi and J. Papavassiliou, Phys. Rep. **479**, 1 (2009).
[17] J. Rodriguez-Quintero, Phys. Rev. D **83**, 097501 (2011).
[18] J. Rodriguez-Quintero, J. High Energy Phys. 01 (2011) 105.
[19] Ph. Boucaud, M. E. Gomez, J. P. Leroy, A. Le Yaouanc, J. Micheli, O. Pene, and J. Rodriguez-Quintero, Phys. Rev. D **82**, 054007 (2010).
[20] Ph. Boucaud, F. De Soto, J. P. Leroy, A. Le Yaouanc, J. Micheli, O. Pene, and J. Rodriguez-Quintero, Phys. Rev. D **79**, 014508 (2009).
[21] P. Boucaud, J-P. Leroy, A. L. Yaouanc, J. Micheli, O. Pene, and J. Rodriguez-Quintero, J. High Energy Phys. 06 (2008) 012.
[22] C. S. Fischer, A. Maas, and J. M. Pawlowski, Ann. Phys. (N.Y.) **324**, 2408 (2009).
[23] A. P. Szczepaniak and H. H. Matevosyan, Phys. Rev. D **81**, 094007 (2010).
[24] A. C. Aguilar and A. A. Natale, J. High Energy Phys. 08 (2004) 057.
[25] D. Dudal, J. A. Gracey, S. P. Sorella, N. Vandersickel, and H. Verschelde, Phys. Rev. D **78**, 065047 (2008).
[26] D. Dudal, O. Oliveira, and N. Vandersickel, Phys. Rev. D **81**, 074505 (2010).
[27] D. Dudal, S. P. Sorella, and N. Vandersickel, Phys. Rev. D **84**, 065039 (2011).
[28] K.-I. Kondo, Phys. Rev. D **84**, 061702 (2011).
[29] A. C. Aguilar, D. Binosi, and J. Papavassiliou, Phys. Rev. D **81**, 125025 (2010).
[30] A. C. Aguilar, D. Binosi, and J. Papavassiliou, J. High Energy Phys. 07 (2010) 002.
[31] A. C. Aguilar and J. Papavassiliou, Phys. Rev. D **83**, 014013 (2011).
[32] A. C. Aguilar, D. Binosi, and J. Papavassiliou, J. High Energy Phys. 01 (2012) 050.
[33] A. Cucchieri, D. Dudal, T. Mendes, and N. Vandersickel, Phys. Rev. D **85**, 094513 (2012).
[34] D. Dudal, N. Vandersickel, A. Cucchieri, and T. Mendes, Proc. Sci. QCD-TNT-II (2011) 015.
[35] J. I. Skullerud, P. O. Bowman, A. Kizilersu, D. B. Leinweber, and A. G. Williams, J. High Energy Phys. 04 (2003) 047.
[36] A. Cucchieri, A. Maas, and T. Mendes, Phys. Rev. D **77**, 094510 (2008).
[37] P. Boucaud, D. Dudal, J. P. Leroy, O. Pene, and J. Rodriguez-Quintero, J. High Energy Phys. 12 (2011) 018.
[38] C. S. Fischer and R. Alkofer, Phys. Rev. D **67**, 094020 (2003).
[39] C. S. Fischer, P. Watson, and W. Cassing, Phys. Rev. D **72**, 094025 (2005).
[40] J. M. Cornwall, Phys. Rev. D **26**, 1453 (1982).
[41] J. M. Cornwall and J. Papavassiliou, Phys. Rev. D **40**, 3474 (1989).
[42] D. Binosi and J. Papavassiliou, Phys. Rev. D **66**, 111901 (R) (2002).
[43] D. Binosi and J. Papavassiliou, J. Phys. G **30**, 203 (2004).
[44] See, e.g., L. F. Abbott, Nucl. Phys. **B185**, 189 (1981), and references therein.
[45] D. Binosi and J. Papavassiliou, J. High Energy Phys. 11 (2008) 063.
[46] W. J. Marciano and H. Pagels, Phys. Rep. **36**, 137 (1978).
[47] J. S. Ball and T.-W. Chiu, Phys. Rev. D **22**, 2542 (1980).
[48] D. C. Curtis and M. R. Pennington, Phys. Rev. D **42**, 4165 (1990).
[49] P. A. Grassi, T. Hurth, and A. Quadri, Phys. Rev. D **70**, 105014 (2004).
[50] A. C. Aguilar, D. Binosi, and J. Papavassiliou, J. High Energy Phys. 11 (2009) 066.
[51] A. C. Aguilar, D. Binosi, J. Papavassiliou, and J. Rodriguez-Quintero, Phys. Rev. D **80**, 085018 (2009).
[52] A. Sternbeck, arXiv:hep-lat/0609016.
[53] A. C. Aguilar, D. Binosi, and J. Papavassiliou, Phys. Rev. D **84**, 085026 (2011).
[54] A. C. Aguilar and J. Papavassiliou, Phys. Rev. D **81**, 034003 (2010).
[55] A. C. Aguilar, D. Ibanez, V. Mathieu, and J. Papavassiliou, Phys. Rev. D **85**, 014018 (2012).
[56] L. Del Debbio, Proc. Sci. LATTICE2010 (2010) 004.
[57] X. Cheng and E. T. Tomboulis, Proc. Sci. QCD-TNT-II (2011) 046.
[58] C. D. Roberts and A. G. Williams, Prog. Part. Nucl. Phys. **33**, 477 (1994).
[59] P. Boucaud, J. P. Leroy, J. Micheli, O. Pene, and C. Roiesnel, J. High Energy Phys. 12 (1998) 004.
[60] P. Boucaud, J. P. Leroy, J. Micheli, O. Pene, and C. Roiesnel, J. High Energy Phys. 10 (1998) 017.
[61] P. Boucaud *et al.*, J. High Energy Phys. 04 (2000) 006.
[62] K. G. Chetyrkin and T. Seidensticker, Phys. Lett. B **495**, 74 (2000).
[63] J. D. Bjorken and S. D. Drell, *Relativistic Quantum Fields*, International Series in Pure and Applied Physics (McGraw-Hill, New York, 1965).
[64] D. Binosi and J. Papavassiliou, J. High Energy Phys. 03 (2011) 121.
[65] J. S. Ball and T. W. Chiu, Phys. Rev. D **22**, 2550 (1980); **23**, 3085(E) (1981).
[66] P. A. Grassi, T. Hurth, and M. Steinhauser, Ann. Phys. (N.Y.) **288**, 197 (2001).
[67] F. de Soto and C. Roiesnel, J. High Energy Phys. 09 (2007) 007.
[68] P. Maris and C. D. Roberts, Phys. Rev. C **56**, 3369 (1997).
[69] B. El-Bennich, G. Krein, L. Chang, C. D. Roberts, and D. J. Wilson, Phys. Rev. D **85**, 031502 (2012).
[70] A. Kizilersu and M. R. Pennington, Phys. Rev. D **79**, 125020 (2009); A. Bashir, A. Kizilersu, and M. R. Pennington, Phys. Rev. D **57**, 1242 (1998).
[71] A. Bashir, R. Bermudez, L. Chang, and C. D. Roberts, Phys. Rev. C **85**, 045205 (2012).
[72] A. I. Davydychev, P. Osland, and L. Saks, Phys. Rev. D **63**, 014022 (2000).